https://doi.org/10.5194/wes-2026-183
Preprint. Discussion started: 4 November 2026
© Author(s) 2026. CC BY 4.0 License.

eawe european academy of wind energy
Open Access WIND ENERGY SCIENCE DISCUSSIONS

An analytical wake deflection model for wind farms including secondary wake steering

Nils Joseph Gaukroger[1], Diego Siguenza-Alvarado[2,3], Maarten Paul van der Laan[1], and Majid Bastankhah[2]

[1]Technical University of Denmark, DTU Wind and Energy Systems, Risø Campus, Frederiksborgvej 399, 4000, Roskilde, Denmark
[2]Department of Engineering, Durham University, Durham DH1 3LE, UK
[3]Centro de Energías Renovables y Alternativas, Escuela Superior Politécnica del Litoral (ESPOL), Campus Gustavo Galindo km. 30.5 Vía Perimetral, Guayaquil, 090902, Ecuador

Correspondence: Nils Joseph Gaukroger (njoga@dtu.dk)

Abstract. Wake interactions between turbines are a major source of power loss in wind farms, which yaw-based wake steering seeks to mitigate. Existing steering models commonly superpose single-turbine deficit and deflection models, which can struggle with non-linear phenomena such as secondary wake steering; momentum-conserving models that do capture it rely on iteration or proxies such as effective yaw angles. This paper extends an approximate "conservation of momentum deficit" solution to the lateral direction, giving an analytical, non-iterative model of the cumulative streamwise and lateral velocity deficits in a wind farm of yawed turbines. Distinguishing the streamwise from the lateral wake makes the spatial distribution of lateral momentum induced by yaw misalignment explicit, and wake deflection follows diagnostically by integrating the local skew angle. The framework yields physical insight into secondary wake steering: the wake of an unyawed downstream turbine is deflected not only by the cross-flow of the upstream wakes, but also, for about a third of its deflection, by the turbine's own streamwise deficit slowing the flow that carries that cross-flow. Against wind-tunnel measurements of single- and multi-turbine configurations, the model reproduces the far-wake deflection and lateral velocity distributions, and is more accurate than established engineering models in most configurations; over the full hub-height velocity field – which needs no wake centre and remains well defined where wakes merge – it is the more accurate in every configuration tested. The main discrepancies are confined to the near wake, where the simplified treatment underpredicts the streamwise velocity deficit. Being analytical and non-iterative, the formulation suits wind farm control and optimisation applications that require low-order models.

1 Introduction

As wind farms and wind farm clusters continue to grow, the aerodynamic interaction between turbine wakes has become a dominant source of power loss and additional structural loading (Peña et al., 2018; Schneemann et al., 2020; Thomsen and Sørensen, 1999; Reinwardt et al., 2021). Accurately predicting wake behaviour is therefore increasingly important for both wind farm design and control. Among proposed wind farm control strategies, yaw-based wake steering has emerged as one of the most widely studied approaches. By intentionally yawing an upstream turbine away from the incoming flow direction, the

https://doi.org/10.5194/wes-2026-183
Preprint. Discussion started: 4 November 2026
© Author(s) 2026. CC BY 4.0 License.

eawe european academy of wind energy
Open Access WIND ENERGY SCIENCE DISCUSSIONS

turbine wake can be laterally displaced, potentially increasing the net power output of the wind farm, despite a reduction in the power and an increase in loading of the yawed turbine itself (Fleming et al., 2017, 2018). Realising these benefits depends on low-order engineering wake models that are cheap enough for real-time control, layout optimisation, and co-design while capturing the dominant wake physics. Advancement in these models requires a continued focus on the fundamental physics (Meneveau, 2019).

Early engineering wake steering models focused on single turbines. Jiménez et al. (2010) used large-eddy simulation (LES) to empirically parameterise deflection for a single turbine as a function of yaw angle. These deflected single-turbine wakes could then be combined to simulate a wind farm with yawed turbines using superposition techniques such as linear and root-sum-square. This led to an early popular implementation of a wind farm wake steering model, the multi-zone model, implemented in FLORIS as a combination of the Jiménez wake deflection model and the N.O. Jensen wake deficit model (Gebraad et al., 2016). Later, Bastankhah and Porté-Agel (2016) introduced a single-turbine deflection model for the Gaussian deficit model.

Whilst computationally efficient, these modular approaches became less accurate as wind farms grew larger, as they implicitly assume that wake interactions can be represented as linear or non-linear combinations of otherwise independent wakes, determined solely by the yaw misalignment of the turbine in question. This has come under scrutiny since the publication of studies reporting so-called secondary wake-steering effects that traditional engineering models are unable to capture (Fleming et al., 2018; Zong and Porté-Agel, 2020; Steiner et al., 2026). The term has been used with varying definitions in the literature. King et al. (2021) and Zong and Porté-Agel (2020) define it as the deflection of downstream wakes due to the non-vanishing transverse velocity induced by upstream turbines; we adopt this definition. Several physical mechanisms have been proposed to explain these effects. The most popular is to attribute them to the often kidney-shaped counter-rotating vortex pairs produced by yawed turbines (Howland et al., 2016; Fleming et al., 2018).

Non-linear wake interactions motivated engineering models of the cumulative wake deficit across wind farms. Zong and Porté-Agel (2020, 2021) introduced momentum-conserving formulations for wake deficit based on a mean convection velocity calculated iteratively as a weighted average of the wake velocity. Momentum-conserving formulations are particularly attractive because they allow wake interactions to emerge naturally from the governing transport equations, rather than relying on empirical wake superposition rules. The same approach gives the skew angle of a yawed turbine's wake, the slope of its trajectory, with the lateral convection velocity taken from Shapiro et al. (2018). There are three limitations with this approach. Firstly, the exact solution is iterative, increasing computational expense. Secondly, on the physical side, the solution accounts for advected lateral velocity but underestimates the deflection due to secondary wake steering. The authors attribute this underestimation to partial wakes causing uneven wake recovery rates. Finally, the iterative momentum-conserving superposition method can lead to non-physical convection velocities that exceed the freestream, which requires limiting the superposition weights to be no greater than 1 (van der Laan et al., 2026).

Bastankhah et al. (2021) also proposed a solution for the cumulative wake deficit based on momentum deficit conservation. Combining that solution with the curled-wake model of Martínez-Tossas et al. (2019) and the super-Gaussian near-wake model of Blondel and Cathelain (2020) yields the cumulative curl model, which also captures secondary wake steering in wind farms

https://doi.org/10.5194/wes-2026-183
Preprint. Discussion started: 4 November 2026
© Author(s) 2026. CC BY 4.0 License.

eawe european academy of wind energy
Open Access WIND ENERGY SCIENCE DISCUSSIONS

(Bay et al., 2023). However, the cumulative curl model inherits the effective yaw angle of King et al. (2021): the lateral velocity advected to a downstream turbine is represented by the yaw angle that would produce it at an isolated turbine, so that the deflection is inferred through a proxy rather than calculated from the flow field.

In this study, the momentum-deficit solution of Bastankhah et al. (2021) is extended to the lateral direction, giving an analytical, non-iterative model of the cumulative wake of yawed turbines in a wind farm, with the near wake of Shapiro et al. (2018). Each turbine's lateral velocity is solved for rather than represented by an effective yaw angle, and the deflection follows from the resulting velocity field. The same balance shows where secondary wake steering comes from: the wake of an unyawed turbine is deflected both by the cross-flow of upstream wakes and by its own streamwise deficit, which slows the flow that carries that cross-flow. The remainder of this paper is structured as follows: Section 2 sets out the derivation of the model, starting with the Reynolds-averaged Navier-Stokes (RANS) equations and ending with some physical insights into secondary wake steering; Section 3 then closes the model with the wake deflection and the geometric parameters of the wakes of yawed turbines, before Sect. 4 compares predictions of the model to wind-tunnel results and other models for a range of wind farm layouts; Section 5 then summarises the findings and describes relevant future work. Appendices A–C give the derivation of the lateral closures, pseudocode for the model, and a sensitivity check of the baseline model.

2 Model derivation

Consider a wind farm with an arbitrary layout of n wind turbines, denoted WT_i for $i = 1, 2, \ldots, n$, within a turbulent boundary-layer flow characterised by arbitrary streamwise $U_0(x, y, z)$ and lateral $V_0(x, y, z)$ background velocity fields, as depicted in Fig. 1(a). The rotor centre location of each WT_i is given by coordinates (x_i, y_i, z_i), where x, y, and z represent the streamwise, lateral, and vertical Cartesian coordinates, respectively. The turbines are labelled according to their streamwise position such that $x_i \geq x_{i-1}$, and the coordinate system is aligned with the incoming velocity at hub height such that $V_0(0, y_1, z_1) = 0$. Note also that the turbines in this arbitrary wind farm can have different hub heights.

Bastankhah et al. (2021) derived the integral momentum equation for a turbine in a wind farm in the streamwise direction. Wake steering needs the lateral direction too, so we derive both, in vector form, starting from the RANS equations at high Reynolds numbers for the streamwise and lateral velocity components,

$$\frac{\partial U(\boldsymbol{U}_0 - \boldsymbol{U})}{\partial x} + \frac{\partial V(\boldsymbol{U}_0 - \boldsymbol{U})}{\partial y} + \frac{\partial W(\boldsymbol{U}_0 - \boldsymbol{U})}{\partial z} = \frac{1}{\rho}\boldsymbol{\nabla}_{\mathrm{H}} P + \mathcal{R} + \left(U\frac{\partial \boldsymbol{U}_0}{\partial x} + V\frac{\partial \boldsymbol{U}_0}{\partial y} + W\frac{\partial \boldsymbol{U}_0}{\partial z} \right) - \frac{1}{\rho}\sum_{i=1}^{n} \mathcal{F}_i \boldsymbol{e}_{\gamma_i}, \qquad (1)$$

where $\boldsymbol{\nabla}_{\mathrm{H}} = (\partial/\partial x, \partial/\partial y)$ and $\boldsymbol{U} = (U, V)$ with U, V and W being the time-averaged velocity components in the x, y, and z directions, respectively. The subscript $(\cdot)_0$ represents the background solution, e.g. $\boldsymbol{U}_0$ is the background flow with no turbines present. The Reynolds stress terms are denoted $\mathcal{R}$, P is the time-averaged static pressure, ρ is the air density, $\mathcal{F}_i$ is the total thrust force per unit volume exerted by WT_i. The yaw angle γ_i of WT_i is measured between the rotor normal and the x-axis, and it is taken as positive for a clockwise rotation of the rotor when viewed from above. Assuming the thrust force always acts normal to the rotor plane (Bastankhah and Porté-Agel, 2017), the unit vector for the forcing can be defined as $\boldsymbol{e}_{\gamma_i} = (\cos\gamma_i, -\sin\gamma_i)$, so that a positively yawed turbine deflects its wake towards $+y$, as illustrated in Fig. 1(b). The terms

https://doi.org/10.5194/wes-2026-183
Preprint. Discussion started: 4 November 2026
© Author(s) 2026. CC BY 4.0 License.

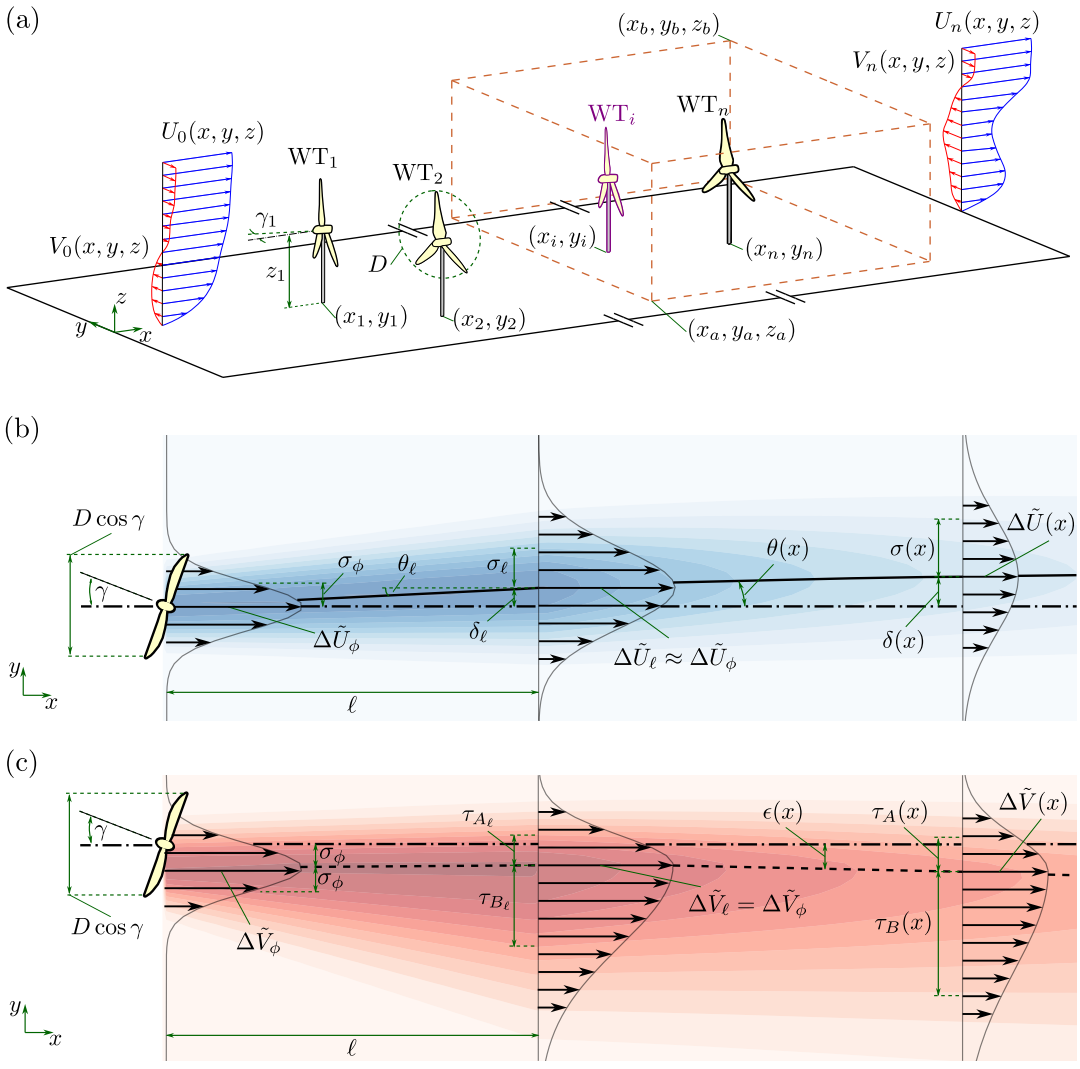

Figure 1. Schematic of: (a) A wind farm with an arbitrary layout of n turbines immersed in a turbulent boundary-layer flow. The dashed red lines represent the control volume integration limits. The integration is performed with and without the highlighted turbine, WT_i. Figure adapted from Bastankhah et al. (2021). (b) The streamwise wake of a yawed turbine within a wind farm, viewed from above, showing the streamwise velocity deficit. The dashed line represents the streamwise wake centre and the dashed-dotted line the rotor centreline. $\Delta\tilde{U}$ is the peak velocity deficit, δ the streamwise wake deflection, σ the characteristic wake width, and θ the wake deflection angle; the subscript ϕ denotes values at the turbine and ℓ values at the onset of the far wake, a distance ℓ downstream of the rotor (Sect. 3). (c) The lateral wake of a yawed turbine within a wind farm, viewed from above, showing the lateral velocity surplus, with the lateral wake centre and the rotor centreline drawn as in (b). $-\Delta\tilde{V}$ is the peak surplus, ϵ the lateral wake deflection, and τ_A, τ_B the characteristic widths of the deflection and non-deflection sides of the wake.

https://doi.org/10.5194/wes-2026-183
Preprint. Discussion started: 4 November 2026
© Author(s) 2026. CC BY 4.0 License.

eawe european academy of wind energy
Open Access WIND ENERGY SCIENCE DISCUSSIONS

$U_i\,\partial \boldsymbol{U}_0/\partial x_i$ represent an inhomogeneous background flow, due for example to complex terrain or gravity waves (Politis et al., 2012; Allaerts and Meyers, 2017); assuming, as is often the case for flat terrain, that its spatial variation is much smaller than that caused by the turbines, they are neglected (Porté-Agel et al., 2020; Bastankhah et al., 2021).

By subtracting the integral of Eq. (1) over the control volume shown in Fig. 1(a), including WT_i, from the integral over the control volume without it, we can derive the following 'conservation of momentum deficit' equation (derived in detail by Bastankhah et al., 2021):

$$\rho \int U_{1:i}\,(\boldsymbol{U}_0 - \boldsymbol{U}_{1:i})\,\mathrm{d}A - \rho \int U_{1:i-1}\,(\boldsymbol{U}_0 - \boldsymbol{U}_{1:i-1})\,\mathrm{d}A \approx T_i \boldsymbol{e}_{\gamma_i}, \tag{2}$$

where $\mathrm{d}A$ is $\mathrm{d}y\,\mathrm{d}z$ and T_i is the normal thrust force exerted by WT_i, defined as

$$T_i = \frac{\pi \rho D^2}{8} \langle U_{1:i-1} \rangle^2_{(i,x_i)} C_{T,i}\,, \tag{3}$$

where D is the rotor diameter and $C_{T,i}$ is the thrust coefficient of WT_i. Here and hereafter, a subscript $1:j$ denotes a quantity in the presence of $\mathrm{WT}_1, \mathrm{WT}_2, \ldots, \mathrm{WT}_j$, and $\langle\rangle_{(j,x_i)}$ an average over the frontal projected area of WT_j at $x = x_i$, so that $\langle U_{1:i-1} \rangle_{(i,x_i)}$ is the rotor-averaged incoming velocity of WT_i. Its projection onto the rotor normal enters only through the $\cos^{1.8}\gamma_i$ derating of $C_{T,i}$, which was calibrated at zero cross-flow. The further contribution of a local cross-flow, $-\langle V_{1:i-1} \rangle_{(i,x_i)} \sin\gamma_i$, which vanishes for an unyawed rotor, is neglected; in the cases of Sect. 4 it amounts to at most $5\,\%$ of the thrust and under $2\,\%$ of the predicted deflection of any turbine. The momentum-deficit approximation is supported by the LES control-volume budgets of Bastankhah et al. (2021), in which the integrated momentum deficit dominates the streamwise momentum balance, especially in the far wake, and the pressure, Reynolds-stress and mean-shear terms are comparatively negligible.

Within a wind farm, the lateral velocities of different turbines interact, so they cannot be treated only as a means of determining the deflection (Sect. 1). We therefore distinguish the 'streamwise wake', Fig. 1(b), from the 'lateral wake', Fig. 1(c), which carries the surplus lateral momentum induced by a turbine. The streamwise wake is characterised by its deflection δ and width σ, and the lateral wake, which is asymmetric, by its deflection ϵ and the widths τ_A and τ_B of its deflection and non-deflection sides (defined below), both deflections being measured from the rotor centreline. The two wakes need not coincide, and it is the lateral wake that the solution of Eq. (2) for $V_{1:i}$ requires.

As for the streamwise deficit (Bastankhah et al., 2021), a lateral deficit defined relative to the incoming velocity at the turbine would mislead within a wind farm: behind a yawed turbine, the local incoming lateral velocity differs from the V_0 to which the flow eventually recovers. We therefore define the deficit as the difference between the flow in the presence and in the absence of the given turbine (Bastankhah et al., 2021). This presumes that a turbine influences the flow only downstream of its rotor: the induction upstream of the rotor and the associated blockage within the array are neglected throughout. In vector form,

$$\Delta \boldsymbol{U}_{1:i}(\boldsymbol{X}) = \boldsymbol{U}_{1:i-1}(\boldsymbol{X}) - \boldsymbol{U}_{1:i}(\boldsymbol{X}), \tag{4}$$

where $\boldsymbol{X} = (x, y, z)$ denotes a position downwind of WT_i. The streamwise thrust extracts momentum and so creates a deficit, whereas the lateral thrust adds lateral momentum; for consistency of the vector notation, we nevertheless define ΔV as a deficit, so that the physical lateral surplus is $-\Delta V$.

https://doi.org/10.5194/wes-2026-183
Preprint. Discussion started: 4 November 2026
© Author(s) 2026. CC BY 4.0 License.

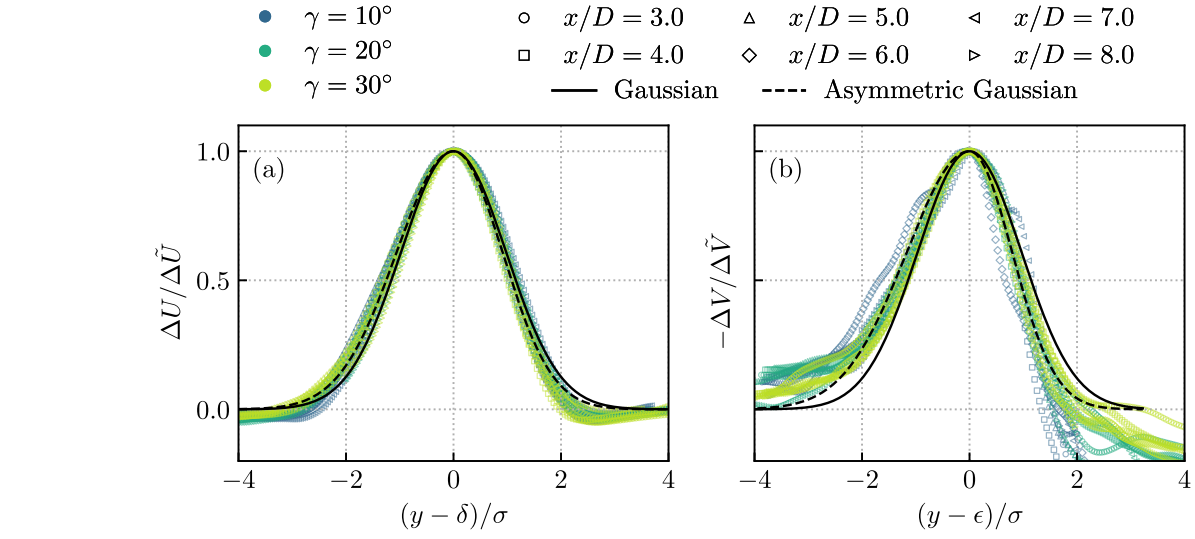

Figure 2. Self-similar profiles of (a) normalised streamwise velocity deficit and (b) normalised lateral velocity surplus for yaw angles of 10°, 20°, and 30° at downstream distances of $x/D = 3, 4, 5, 6, 7, 8$, based on wind tunnel data from Bastankhah and Porté-Agel (2016). The streamwise and lateral wake deflections, denoted δ and ϵ, respectively, are the offsets of the profile maximum from the rotor centreline, as defined in Fig. 1(b) and (c). The wake width, σ, is computed using the generalised integral in Eq. (4.1) of Bastankhah and Porté-Agel (2016).

To derive a solution for $V_{1:i}$, we assume that the velocity profiles in turbine wakes within wind farms are self-similar. The far-wake streamwise deficit of a yawed turbine is self-similar (Fig. 2(a)), and the far-wake lateral surplus shows a good degree of self-similarity over a range of yaw angles (Fig. 2(b)), so that it too can be given a generalised functional form. That form cannot be the Gaussian of the streamwise deficit: Fig. 2 compares each profile with an asymmetric Gaussian, which has an independent half-width on each side of its centre, and whilst the streamwise profile is nearly symmetric, the lateral one is markedly asymmetric.

The asymmetry follows from the physics of the lateral wake. Behind an unyawed turbine, wake recovery draws the flow towards the rotor centreline from both sides (Fig. 3(a)), giving an approximately antisymmetric profile (Fig. 3(c)). Behind a yawed turbine, the lateral thrust induces a lateral velocity of one sign across the wake, which grows with the yaw angle (Fig. 3(b),(c)). The two combine constructively on one side of the wake and destructively on the other, producing both the asymmetry and the negative velocities of Fig. 2(b). Beyond the hub-height plane, the counter-rotating vortex pair of a yawed wake (Bastankhah and Porté-Agel, 2016; Howland et al., 2016; Bastankhah et al., 2022) adds a three-dimensional structure that may also contribute to the asymmetry. Figure 3(b) also shows that the streamwise wake centre, δ, and the lateral wake centre, ϵ, lie on opposite sides of the rotor centreline, so the deflection is evaluated away from the peak of the lateral surplus. We call the side of the lateral wake on which the streamwise centre lies, $(y-\epsilon)/\sigma > 0$ in Fig. 2(b), the 'deflection' side, and the other the 'non-deflection' side.

https://doi.org/10.5194/wes-2026-183
Preprint. Discussion started: 4 November 2026
© Author(s) 2026. CC BY 4.0 License.

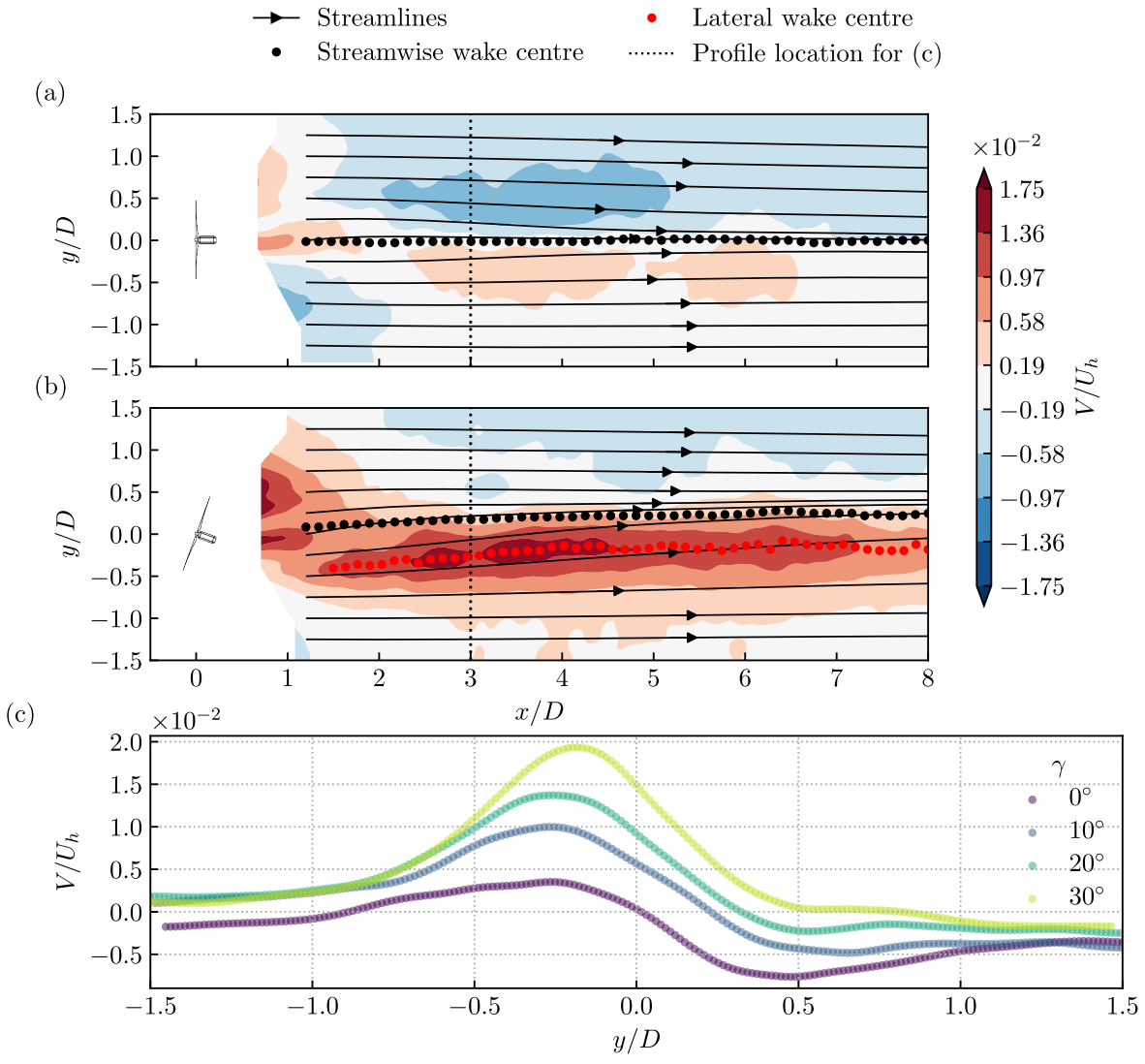

Figure 3. Contours of lateral velocity normalised by hub-height streamwise velocity with streamlines for (a) an unyawed turbine and (b) a turbine yawed to 20° in a plane at hub height downstream of the rotor, shown with centre at $(0,0)$. (c) Profiles of lateral velocity normalised by streamwise hub-height inflow velocity for various yaw angles at a downstream distance of $x/D = 3.0$, based on wind tunnel data from Bastankhah and Porté-Agel (2016); the rotor centre is located at $y = 0$.

https://doi.org/10.5194/wes-2026-183
Preprint. Discussion started: 4 November 2026
© Author(s) 2026. CC BY 4.0 License.

eawe european academy of wind energy
Open Access WIND ENERGY SCIENCE DISCUSSIONS

Even the asymmetric Gaussian departs from the measurements in two ways. Firstly, there are negative velocities for $(y-\epsilon)/\sigma > 0$, particularly at small yaw angles. Although hidden by the normalisation, the lateral surpluses at small yaw angles are up to two orders of magnitude smaller than the streamwise deficits, so modelling these negative velocities is considered unnecessary complexity, and the surplus is assumed to be positive; this amounts to assuming that the recovery is much weaker than the lateral forcing. Secondly, for $(y-\epsilon)/\sigma < -2$, the measurements retain a tail at some 7–20 % of the peak surplus that persists to at least 4σ, and which no Gaussian, symmetric or asymmetric, can reproduce. Both departures are confined to the flanks: within about 2σ of the lateral wake centre the asymmetric Gaussian tracks the data to within roughly 5 % of the peak, whereas beyond that distance it lies above the measurements on one side – where the measured surplus changes sign, at $(y-\epsilon)/\sigma \approx 1.8$ – and below them on the other. The streamwise centre lies well within 2σ of the lateral centre, so these departures do not affect the deflection of an isolated turbine. Within a wind farm, however, a downstream rotor may lie on either flank of an upstream lateral wake, where the lateral velocity it inherits sets much of its own deflection; Sect. 4.2.2 returns to this for the staggered layouts.

We were unable to find data suitable for testing the far-wake self-similarity of lateral wakes within wind farms. Far-wake self-similarity of the streamwise wake has, however, been demonstrated for isolated turbines and often carries over to the wind-farm setting (Bastankhah et al., 2021), so we assume the same of the lateral wake. The velocity deficit due to WT_i is then

$$\Delta \boldsymbol{U}_i(\boldsymbol{X}) = \boldsymbol{U}_{1:i-1}(\boldsymbol{X}) - \boldsymbol{U}_{1:i}(\boldsymbol{X}) = \Delta\tilde{\boldsymbol{U}}_i(x)\boldsymbol{f}_i(\boldsymbol{X}), \tag{5}$$

where $\Delta\tilde{\boldsymbol{U}}_i = (\Delta\tilde{U}_i, \Delta\tilde{V}_i)$ denotes the peak velocity deficit components caused by WT_i and $\boldsymbol{f}_i = (f_i, g_i)$ the normalised self-similar spatial distributions for the streamwise and lateral velocity deficits, respectively. Vector products such as $\Delta\tilde{\boldsymbol{U}}_i\boldsymbol{f}_i$ are understood componentwise throughout, i.e. $\Delta\tilde{\boldsymbol{U}}_i\boldsymbol{f}_i = (\Delta\tilde{U}_i f_i,\ \Delta\tilde{V}_i g_i)$. This relationship can be applied to all previous turbines by shifting the indices backwards, which yields a set of equations:

$$\begin{aligned}
\boldsymbol{U}_{1:i-2} - \boldsymbol{U}_{1:i-1} &= \Delta\tilde{\boldsymbol{U}}_{i-1}\boldsymbol{f}_{i-1} \\
\boldsymbol{U}_{1:i-3} - \boldsymbol{U}_{1:i-2} &= \Delta\tilde{\boldsymbol{U}}_{i-2}\boldsymbol{f}_{i-2} \\
&\vdots \\
\boldsymbol{U}_0 - \boldsymbol{U}_1 &= \Delta\tilde{\boldsymbol{U}}_1\boldsymbol{f}_1.
\end{aligned} \tag{6}$$

Adding Eq. (5) to Eq. (6) then results in

$$\boldsymbol{U}_0 - \boldsymbol{U}_{1:i} = \sum_{j=1}^{i} \Delta\tilde{\boldsymbol{U}}_j(x)\boldsymbol{f}_j(x,y,z). \tag{7}$$

i.e. the cumulative velocity deficit across the wind farm with respect to the inflow velocity $\boldsymbol{U}_0$. Substituting it into Eq. (2) gives

$$\rho \int \left(U_0 \Delta\tilde{\boldsymbol{U}}_i\boldsymbol{f}_i - \Delta\tilde{U}_i f_i \sum_{j=1}^{i-1} \Delta\tilde{\boldsymbol{U}}_j\boldsymbol{f}_j - \Delta\tilde{\boldsymbol{U}}_i\boldsymbol{f}_i \sum_{j=1}^{i-1} \Delta\tilde{U}_j f_j - \Delta\tilde{U}_i f_i \Delta\tilde{\boldsymbol{U}}_i\boldsymbol{f}_i \right) \mathrm{d}A \approx T_i \boldsymbol{e}_{\gamma_i}. \tag{8}$$

https://doi.org/10.5194/wes-2026-183
Preprint. Discussion started: 4 November 2026
© Author(s) 2026. CC BY 4.0 License.

eawe european academy of wind energy
Open Access WIND ENERGY SCIENCE DISCUSSIONS

Here $\Delta\tilde{U}_i f_i$, without vector notation, is the streamwise contribution of WT_i itself: the equation is solved first in the streamwise direction, and $\Delta\tilde{U}_i$ then enters the lateral direction as a known scalar. For the streamwise velocity deficit, we use a Gaussian profile as the self-similar distribution, such that

$$f_i = \exp\left(-\frac{(y-(y_i+\delta_i))^2+(z-z_i)^2}{2\sigma_i^2}\right), \tag{9}$$

where δ_i and σ_i are the deflection and characteristic width of the streamwise wake of WT_i. This allows us to solve Eq. (8) in the streamwise direction for $\Delta\tilde{U}_i$ as

$$\frac{\Delta\tilde{U}_i}{U_h} = \left(1-\sum_{j=1}^{i-1}\lambda_{ij}\frac{\Delta\tilde{U}_j}{U_h}\right)\left(1-\sqrt{1-\frac{C_{T,i}\cos\gamma_i\left(\frac{\langle U_{1:i-1}\rangle_{(i,x_i)}}{U_h}\right)^2}{8\left(\frac{\sigma_i}{D}\right)^2\left(1-\sum_{j=1}^{i-1}\lambda_{ij}\frac{\Delta\tilde{U}_j}{U_h}\right)^2}}\right), \tag{10}$$

where $U_h = U_0|_{z=z_h}$ is the inflow velocity at the reference hub height z_h, and the dimensionless coefficient, λ_{ij}, which quantifies the contribution of WT_j to the value of $\Delta\tilde{U}_i$, is given by

$$\lambda_{ij} = \frac{\alpha\sigma_j^2}{\sigma_i^2+\sigma_j^2}\exp\left(-\frac{((y_i+\delta_i)-(y_j+\delta_j))^2}{2\left(\sigma_i^2+\sigma_j^2\right)}\right)\exp\left(-\frac{(z_i-z_j)^2}{2\left(\sigma_i^2+\sigma_j^2\right)}\right), \tag{11}$$

where $\alpha = 2$ is the exact solution of Eq. (2). Bastankhah et al. (2021) used $\alpha = 1$ to account for terms neglected in the derivation; we retain the exact value.

With $\Delta\tilde{U}_i$ known from Eq. (10), the lateral component of Eq. (2) reads

$$\int U_{1:i}\,(V_0 - V_{1:i})\,\mathrm{d}A - \int U_{1:i-1}\,(V_0 - V_{1:i-1})\,\mathrm{d}A \approx -\frac{T_i\sin\gamma_i}{\rho}. \tag{12}$$

By Eq. (5), $U_{1:i} = U_{1:i-1} - \Delta\tilde{U}_i f_i$ and $V_{1:i} = V_{1:i-1} - \Delta\tilde{V}_i g_i$, which separates the contribution of WT_i from that of everything upstream of it, and by Eq. (7) the upstream turbines leave $V_0 - V_{1:i-1} = \sum_{j=1}^{i-1}\Delta\tilde{V}_j g_j$. The left-hand side of Eq. (12) is therefore

$$\Delta\tilde{V}_i\int U_{1:i}\,g_i\,\mathrm{d}A - \Delta\tilde{U}_i\sum_{j=1}^{i-1}\Delta\tilde{V}_j\int f_i\,g_j\,\mathrm{d}A, \tag{13}$$

which, equated to its right-hand side, leaves the balance

$$\Delta\tilde{V}_i K_i = S_i + Q_i, \quad \text{where} \quad K_i = \int U_{1:i}\,g_i\,\mathrm{d}A, \quad S_i = -\frac{T_i\sin\gamma_i}{\rho}, \quad \text{and} \quad Q_i = \Delta\tilde{U}_i\sum_{j=1}^{i-1}\Delta\tilde{V}_j\int f_i\,g_j\,\mathrm{d}A. \tag{14}$$

In words, the peak lateral velocity deficit times K_i, the streamwise mass flux (per unit density) through the lateral wake, equals the lateral thrust S_i plus the inherited lateral momentum Q_i. The upstream wakes leave a *cross-flow* at WT_i, the lateral velocity $\sum_{j=1}^{i-1}\Delta\tilde{V}_j g_j$ of the turbines upstream of it, which the freestream does not have and which carries a lateral momentum flux.

https://doi.org/10.5194/wes-2026-183
Preprint. Discussion started: 4 November 2026
© Author(s) 2026. CC BY 4.0 License.

eawe european academy of wind energy
Open Access WIND ENERGY SCIENCE DISCUSSIONS

The streamwise wake of WT_i reduces that flux by Q_i, the second term of Eq. (13). The lateral thrust is the only source of lateral momentum, so the reduction cannot simply be lost: the wake of WT_i must carry it instead, at a higher lateral velocity through a smaller mass flux. Substituting the streamwise component of Eq. (7) for $U_{1:i}$, the mass flux is

$$K_i = \int U_0\, g_i \,\mathrm{d}A - \sum_{j=1}^{i-1} \Delta\tilde{U}_j \int f_j\, g_i \,\mathrm{d}A - \Delta\tilde{U}_i \int f_i\, g_i \,\mathrm{d}A, \tag{15}$$

i.e. the freestream mass flux less the parts removed where the streamwise wakes of upstream turbines and of WT_i itself overlap the lateral wake; any reduction raises $|\Delta\tilde{V}_i|$ for the same forcing.

Evaluating these integrals requires a function for g_i. Following Fig. 2(b), we take an asymmetric Gaussian, which can be written as

$$g_i = \begin{cases} \exp\left(-\frac{(y-(y_i+\epsilon_i))^2}{2\tau_{A_i}^2}\right)\exp\left(-\frac{(z-z_i)^2}{2\tau_{A_i}^2}\right) = g_{A_i}, & \text{for} \quad s_i\,(y-(y_i+\epsilon_i)) \geq 0 \quad \text{and} \\ \exp\left(-\frac{(y-(y_i+\epsilon_i))^2}{2\tau_{B_i}^2}\right)\exp\left(-\frac{(z-z_i)^2}{2\tau_{B_i}^2}\right) = g_{B_i}, & \text{for} \quad s_i\,(y-(y_i+\epsilon_i)) < 0\,, \end{cases} \tag{16}$$

where the lateral wake centre lies at $y_i+\epsilon_i$, the location of the peak surplus $-\Delta\tilde{V}_i$, and τ_{A_i} and τ_{B_i} are the widths of the deflection and non-deflection sides (Fig. 1(c)). The side is set by the deflection-side sign

$$s_i = \begin{cases} \mathrm{sgn}\,(\gamma_i)\,, & \gamma_i \neq 0, \\ \mathrm{sgn}\,(V_{\mathrm{local},i})\,, & \gamma_i = 0, \end{cases} \tag{17}$$

the side to which the wake of WT_i is deflected. An unyawed turbine exerts no lateral thrust, but its wake may still be deflected by the upstream cross-flow, whose direction at its hub, $V_{\mathrm{local},i}$, then sets the side; since ϵ_i is constructed with the same sign (Eq. (32)), $s_i = \mathrm{sgn}(\delta_i - \epsilon_i)$. Substituting this g_i into Eq. (14) with $U_0 = U_h$, we can integrate analytically and, dividing by $\pi D^2 U_h^2$, obtain

$$\frac{\Delta\tilde{V}_i}{U_h} = \frac{\mathcal{S}_i + \mathcal{Q}_i}{\mathcal{K}_i}, \tag{18}$$

the dimensionless form of Eq. (14), in which

$$\mathcal{K}_i = \frac{K_i}{\pi D^2 U_h} = \underbrace{\left(\frac{\tau_{A_i}}{D}\right)^2 + \left(\frac{\tau_{B_i}}{D}\right)^2}_{\text{freestream}} - \underbrace{\sum_{j=1}^{i-1} \frac{\Delta\tilde{U}_j}{U_h}\left(\frac{\sigma_j}{D}\right)^2 \mu_{ji}}_{\text{upstream wakes}} - \underbrace{\frac{\Delta\tilde{U}_i}{U_h}\left(\frac{\sigma_i}{D}\right)^2 \mu_{ii}}_{\text{own wake}},$$

$$\mathcal{S}_i = \frac{S_i}{\pi D^2 U_h^2} = -\left(\frac{C_{T,i}}{8}\right)\left(\frac{\langle U_{1:i-1}\rangle_{(i,x_i)}}{U_h}\right)^2 \sin\gamma_i, \tag{19}$$

$$\mathcal{Q}_i = \frac{Q_i}{\pi D^2 U_h^2} = \frac{\Delta\tilde{U}_i}{U_h}\left(\frac{\sigma_i}{D}\right)^2 \sum_{j=1}^{i-1} \frac{\Delta\tilde{V}_j}{U_h}\mu_{ij},$$

https://doi.org/10.5194/wes-2026-183
Preprint. Discussion started: 4 November 2026
© Author(s) 2026. CC BY 4.0 License.

eawe european academy of wind energy
Open Access WIND ENERGY SCIENCE DISCUSSIONS

the three terms of $\mathcal{K}_i$ being the three of Eq. (15) in order and μ_{ij} the dimensionless coefficient

$$\mu_{ij} = \left[1 + \operatorname{erf}\left(\eta_{A,ij}\right)\right] \frac{\tau_{A_j}^2}{\sigma_i^2 + \tau_{A_j}^2} \exp\left(-\frac{d_{ij}^2 + \left(z_i - z_j\right)^2}{2\left(\sigma_i^2 + \tau_{A_j}^2\right)}\right) + \left[1 - \operatorname{erf}\left(\eta_{B,ij}\right)\right] \frac{\tau_{B_j}^2}{\sigma_i^2 + \tau_{B_j}^2} \exp\left(-\frac{d_{ij}^2 + \left(z_i - z_j\right)^2}{2\left(\sigma_i^2 + \tau_{B_j}^2\right)}\right), \tag{20}$$

$$d_{ij} = \left(y_i + \delta_i\right) - \left(y_j + \epsilon_j\right), \qquad \eta_{X,ij} = \frac{s_j\, d_{ij}\, \tau_{X_j}}{\sigma_i \sqrt{2\left(\sigma_i^2 + \tau_{X_j}^2\right)}}, \quad X \in \{A, B\}.$$

Each term is the integral of $f_i g_j$ over one side of the lateral centre $y_j + \epsilon_j$, the side being set by s_j as in Eq. (16). The product of the two Gaussians is again a Gaussian, and the bracket $1 \pm \operatorname{erf}(\eta_{X,ij})$ is twice the fraction of it lying on side X; it reduces to unity only when the streamwise centre lies on the lateral centre, $d_{ij} = 0$. The same expression gives μ_{ji} and μ_{ii} on relabelling, and the brackets matter most for the latter: a turbine's own streamwise and lateral centres lie one width apart by construction, $d_{ii} = s_i \sigma_i$ (Eq. (32)).

Both coefficients are purely geometric, describing how the component wakes of two turbines overlap. The λ_{ij} of Eq. (11), for two symmetric streamwise wakes, is the special case of μ_{ij} for which $\tau_A = \tau_B = \sigma$ and $\epsilon = \delta$: the two brackets then sum to two, which recovers $\alpha = 2$.

Since the convecting velocity is streamwise and already known, $\Delta\tilde{V}_i$ enters the balance once, linearly, with the single coefficient K_i, and so divides uniquely by forcing into a thrust-driven and an inherited component,

$$\frac{\Delta\tilde{V}_i^{\mathrm{thr}}}{U_h} = \frac{\mathcal{S}_i}{\mathcal{K}_i} \tag{21}$$

and

$$\frac{\Delta\tilde{V}_i^{\mathrm{inh}}}{U_h} = \frac{\mathcal{Q}_i}{\mathcal{K}_i} = \frac{\Delta\tilde{V}_i}{U_h} - \frac{\Delta\tilde{V}_i^{\mathrm{thr}}}{U_h}. \tag{22}$$

The sum is exact by construction. Both divide by the same $\mathcal{K}_i$, the mass flux of the turbine as it stands in the farm, upstream term included; with the farm's inflow and wake widths in $\mathcal{S}_i$ besides, the thrust-driven component is not the lateral velocity of an isolated turbine, and no comparison with one is made. For an unyawed turbine $\mathcal{S}_i = 0$, and the whole amplitude is inherited; it needs a yawed turbine upstream, without which there is no cross-flow to inherit.

The effect is non-linear: every farm term in Eq. (18) is a product of a streamwise and a lateral deficit, $Q_i \propto \Delta\tilde{U}_i \Delta\tilde{V}_j$ and the two mass-flux reductions of Eq. (15) contributing $\Delta\tilde{U}_j \Delta\tilde{V}_i$ and $\Delta\tilde{U}_i \Delta\tilde{V}_i$. Linearising, $U_{1:i} \approx U_0$, drops them all and leaves

$$\Delta\tilde{V}_i \approx \frac{S_i}{\int U_0\, g_i \,\mathrm{d}A}, \tag{23}$$

which vanishes for an unyawed turbine. The inherited component thus contributes to the *secondary wake steering* identified elsewhere in the literature (Fleming et al., 2018).

https://doi.org/10.5194/wes-2026-183
Preprint. Discussion started: 4 November 2026
© Author(s) 2026. CC BY 4.0 License.

eawe european academy of wind energy
Open Access WIND ENERGY SCIENCE DISCUSSIONS

The streamwise balance has a single forcing and is quadratic in $\Delta\tilde{U}_i$, so it can be split only by equation: $\Delta\tilde{U}_i^{\mathrm{self}}$ is Eq. (10) without its upstream sums, as used in the near-wake switch of Eq. (28), and $\Delta\tilde{U}_i^{\mathrm{int}} = \Delta\tilde{U}_i - \Delta\tilde{U}_i^{\mathrm{self}}$ is the remainder; this split is not propagated into the deflection. Section 3 shows how the lateral components enter the skew angle of Eq. (29), and Sect. 4.2.1 their contributions to the deflection.

3 Wake deflection and geometry

This section closes the model. It gives the transport law that sets the wake deflection δ, and the closures for the remaining geometric parameters introduced in Sect. 2 and shown in Fig. 1: the streamwise width σ, the lateral widths τ_A and τ_B, and the lateral wake centre ϵ.

The streamwise wake deflection (skew) angle is given by

$$\theta = \frac{\mathrm{d}\delta}{\mathrm{d}x} = \arctan\left(\frac{V}{U}\right) \approx \frac{V}{U}. \tag{24}$$

Taking the wake of each turbine to be undeflected at its rotor, $\delta_i|_{x=x_i} = 0$, Eq. (24) is integrated downstream. As V and U are themselves functions of δ, this is an initial value problem, which we solve by explicit Euler integration in x. Deflection is therefore a non-local quantity: unlike the far-wake velocity, it depends on V/U all the way from the rotor, so any inaccuracy in the near wake, where this ratio is largest, propagates downstream. The near-wake flow is dominated by the turbine in question (Crespo et al., 1999; Lignarolo et al., 2014) and relatively unaffected by the wakes of upstream turbines, so a single-turbine near-wake model suffices for every turbine in the farm. Given that the focus of this paper is the far wake, we use the simple model of Shapiro et al. (2018), such that

$$\frac{\Delta\tilde{U}_{i,\mathrm{nw}}}{U_h} = 2a_i \frac{\langle U_{1:i-1}\rangle_{(i,x_i)}}{U_h}, \tag{25}$$

where a_i is the induction factor, which can be calculated from the thrust coefficient as

$$a_i = \frac{1}{2}\left(1 - \sqrt{1 - C_{T,i}}\right), \tag{26}$$

and

$$\frac{\Delta\tilde{V}_{i,\mathrm{nw}}}{U_h} = -\frac{1}{4} C_{T,i} \frac{\langle U_{1:i-1}\rangle_{(i,x_i)}}{U_h} \sin\gamma_i. \tag{27}$$

Equation (27) differs from Eq. (2.7) of Shapiro et al. (2018) only through the definition of the thrust coefficient. These near-wake values are applied wherever the far-wake self-deficit from Eq. (10) would exceed the near-wake value, i.e. the streamwise self-deficit criterion

$$\chi_i^{\mathrm{nw}}(x) \equiv (x \geq x_i) \wedge \left(\Delta\tilde{U}_i^{\mathrm{far,self}}(x) > \Delta\tilde{U}_{i,\mathrm{nw}}\right), \tag{28}$$

and this same switch is used for the streamwise, lateral and deflection branches. Within the near wake the turbine is treated as if it were alone: the upstream contributions to its peak amplitudes are suppressed ($\Delta\tilde{U}_i^{\mathrm{int}} = \Delta\tilde{V}_i^{\mathrm{inh}} = 0$), and the totals, which

https://doi.org/10.5194/wes-2026-183
Preprint. Discussion started: 4 November 2026
© Author(s) 2026. CC BY 4.0 License.

eawe european academy of wind energy
Open Access WIND ENERGY SCIENCE DISCUSSIONS

are then the single-turbine streamwise and the thrust-driven lateral amplitudes, are capped by Eqs. (25) and (27). With these definitions, we can now write an equation for the skew angle as

$$\theta_i = \begin{cases} \arctan\left(\dfrac{-\Delta\tilde{V}_i \exp\left(-\dfrac{\sigma_i^2}{2\tau_{A_i}^2}\right)}{U_{h,i} - \Delta\tilde{U}_i}\right), & \text{if } \chi_i^{\mathrm{nw}}(x) = 1 \text{ (near wake)}, \\ \arctan\left(\dfrac{V_0(x, y_i+\delta_i, z_i) - \sum_{j=1}^{i} \Delta\tilde{V}_j \exp\left(-\dfrac{((y_j+\epsilon_j)-(y_i+\delta_i))^2 + (z_j - z_i)^2}{2\tau_{\eta_j}^2}\right)}{U_{h,i} - \sum_{j=1}^{i} \Delta\tilde{U}_j \exp\left(-\dfrac{((y_j+\delta_j)-(y_i+\delta_i))^2 + (z_j - z_i)^2}{2\sigma_j^2}\right)}\right), & \text{otherwise}, \end{cases} \tag{29}$$

where $U_{h,i} = U_0|_{z=z_i}$ is the inflow velocity at the hub height of WT_i, and τ_{η_j} is the width of the side of the lateral wake of WT_j on which $y = y_i + \delta_i$ falls, selected as in Eq. (16). For $j = i$ it is always τ_{A_i}, since $s_i(\delta_i - \epsilon_i) = \sigma_i > 0$. Deflection is thus not prescribed but emerges diagnostically from the velocity field.

Let U_i^{up} and V_i^{up} be the denominator and numerator of the far-wake branch with both sums truncated at $j = i-1$, i.e. the flow of the upstream turbines alone at the wake centreline, so that $U_i = U_i^{\mathrm{up}} - \Delta\tilde{U}_i$ and $V_i = V_i^{\mathrm{up}} + V_i^{\mathrm{own}}$, with $V_i^{\mathrm{own}} = -\Delta\tilde{V}_i \exp(-\sigma_i^2/2\tau_{A_i}^2)$. Changing first U_i^{up} and then V_i^{up} to its full value attributes the far-wake skew angle exactly:

$$\begin{aligned} \theta_i &= \underbrace{\arctan\frac{V_i^{\mathrm{up}}}{U_i^{\mathrm{up}}}}_{\theta_i^{\mathrm{tr}}} + \underbrace{\left(\arctan\frac{V_i^{\mathrm{up}}}{U_i} - \arctan\frac{V_i^{\mathrm{up}}}{U_i^{\mathrm{up}}}\right)}_{\theta_i^{\mathrm{car}}} + \underbrace{\left(\arctan\frac{V_i}{U_i} - \arctan\frac{V_i^{\mathrm{up}}}{U_i}\right)}_{\theta_i^{\mathrm{own}}} \\ &\approx \frac{V_i^{\mathrm{up}}}{U_i^{\mathrm{up}}} + V_i^{\mathrm{up}}\left(\frac{1}{U_i} - \frac{1}{U_i^{\mathrm{up}}}\right) + \frac{V_i^{\mathrm{own}}}{U_i}, \end{aligned} \tag{30}$$

the second line being its small-angle form. By share of V_i^{own} between Eqs. (21) and (22), the own-lateral term splits as $\theta_i^{\mathrm{thr}} = (\Delta\tilde{V}_i^{\mathrm{thr}}/\Delta\tilde{V}_i)\,\theta_i^{\mathrm{own}}$ and $\theta_i^{\mathrm{inh}} = \theta_i^{\mathrm{own}} - \theta_i^{\mathrm{thr}}$.

The tracer angle θ_i^{tr} is that of a passive tracer released at the rotor into the upstream flow: Eq. (29) in the limit $C_{T,i} \to 0$, along the same centreline. The carrier angle θ_i^{car} is the extra turning of that cross-flow because the wake is slower than its surroundings: since $\mathrm{d}\delta/\mathrm{d}x \approx V/U$, a slower wake spends longer in the cross-flow per unit streamwise distance. The own-lateral angle θ_i^{own} is the further turning by the lateral velocity the wake itself carries. The inherited part of that lateral velocity, Eq. (22), has the same origin as the carrier angle – the turbine slows the flow – but acts on V rather than on the trajectory: with no lateral thrust to change the flux of Eq. (14), the slower air within the wake must carry a larger lateral velocity, concentrating the cross-flow it stands in rather than creating one. Both are first order in $\Delta\tilde{U}_i$, so their ratio is set by geometry: in the cases of Sect. 4, the inherited angle is about a tenth of the carrier angle. Taking the streamwise step first, as the model solves for $\Delta\tilde{U}_i$ before $\Delta\tilde{V}_i$, is a choice that shares $\theta_i - \theta_i^{\mathrm{tr}}$ between the carrier and own-lateral terms but leaves θ_i^{tr} unchanged. Integrated along x like δ_i, the four components θ_i^{tr}, θ_i^{car}, θ_i^{thr} and θ_i^{inh} partition δ_i exactly.

In the far wake, the skew angle is evaluated from the full velocity field, so each wake is advected by the cross-flow of the wakes upstream of it; evaluating it from the velocities induced by WT_i alone substantially underpredicted the deflection of

https://doi.org/10.5194/wes-2026-183
Preprint. Discussion started: 4 November 2026
© Author(s) 2026. CC BY 4.0 License.

eawe european academy of wind energy
Open Access WIND ENERGY SCIENCE DISCUSSIONS

downstream turbines. The same principle underlies the curled-wake approach, in which downstream deficits are transported by the total transverse velocity field (Martínez-Tossas et al., 2019), and the advected lateral velocity of Zong and Porté-Agel (2020); here it enters analytically, without iteration or an effective yaw angle.

The near-wake branch of Eq. (29) is a deliberate exception, retaining only the turbine's own velocity because the near-wake flow is dominated by the turbine itself; evaluating it from the full summed field substantially overpredicted downstream deflection. That velocity being the thrust-driven solution of Eq. (27), the near-wake skew angle is θ_i^{thr} by construction. Section 4.2.1 reports the four components.

With the skew angle defined, what remains are the wake widths and the lateral wake centre on which it depends. The streamwise width grows linearly with downstream distance from the end of the potential core,

$$\frac{\sigma_\eta}{D} = k_U \frac{x - x_i - x_{0,i}}{D} + \frac{\sigma_{\eta_0}}{D}, \qquad \eta \in \{y, z\}, \qquad \sigma = \sqrt{\sigma_y \sigma_z}, \tag{31}$$

where σ_{y_0} and σ_{z_0} are the lateral and vertical widths at the end of the potential core and $x_{0,i}$ is its length, all from Bastankhah and Porté-Agel (2016) (App. A1). The growth rate is an affine function of the local turbulence intensity, $k_U = 0.38\, I_{\mathrm{local}} + 0.004$ (Niayifar and Porté-Agel, 2016), where $I_{\mathrm{local},i}$ adds to the ambient value the largest added turbulence of the upstream turbines whose wakes overlap the rotor of WT_i. The far wake begins where σ_i reaches the width at which the far- and near-wake solutions for $\Delta\tilde{U}_i$ are equal, so that the switch of Eq. (28) turns off. This onset width, $\sigma_{\ell,i}$, and the distance ℓ_i from the rotor to the onset, at $x_{\chi,i} = x_i + \ell_i$, both have closed forms (App. A1).

The lateral wake centre ϵ follows from the relationship derived by Bastankhah and Porté-Agel (2016, App. A), that $\partial\theta/\partial y = 0$ where $\partial^2 U/\partial y^2 = 0$. With the small-angle approximation, $V \ll U$, the extrema of V therefore lie at the inflection points of U, a reasonable approximation against experimental data (App. A). For the Gaussian deficit of Eq. (9) these are at $y = \delta \pm \sigma$, matching the two extrema of the lateral velocity profiles in Fig. 3(c). We define the lateral wake centre as the one where $|V|$ is greatest, which lies on the side of δ opposite to the deflection. Replacing δ and σ by their values for each turbine, and with the deflection-side sign s_i of Eq. (17),

$$\frac{\epsilon_i}{D} = \frac{\delta_i}{D} - s_i \frac{\sigma_i}{D}. \tag{32}$$

Upstream turbines thus enter ϵ_i implicitly, through δ_i and, via their added turbulence, through σ_i.

For simplicity, we assume that the lateral characteristic wake widths grow linearly with downstream distance, such that

$$\frac{\tau_\eta}{D} = k_{V_\eta} \frac{x - x_{\chi,i}}{D} + \frac{\tau_{\eta\ell}}{D}, \tag{33}$$

where η indicates A or B. This leaves four unknowns, the growth rates k_{V_A} and k_{V_B} and the onset widths τ_{A_ℓ} and τ_{B_ℓ}, which we determine at the far-wake onset, where the near- and far-wake solutions for $\Delta\tilde{U}$ agree by construction (Eq. (A4)). The deflection-side width τ_{A_ℓ} is fixed by requiring that the lateral velocity at the streamwise wake centre, which by Eq. (16) depends on τ_{A_ℓ} alone, reproduces the flow skew angle that Bastankhah and Porté-Agel (2016, Eq. 6.12) give across the potential core,

$$\theta_\ell = \theta_{c_0} = \frac{0.3\gamma}{\cos\gamma}\left(1 - \sqrt{1 - C_T \cos\gamma}\right). \tag{34}$$

https://doi.org/10.5194/wes-2026-183
Preprint. Discussion started: 4 November 2026
© Author(s) 2026. CC BY 4.0 License.

eawe european academy of wind energy
Open Access WIND ENERGY SCIENCE DISCUSSIONS

Taking the near-wake amplitudes of Eqs. (27) and (25) at the onset, with $V_0 = 0$, gives the closed form (App. A)

$$\frac{\tau_{A_\ell}}{D} = \frac{\dfrac{\sigma_\ell}{D}}{\sqrt{2\ln\left(\dfrac{\frac{1}{4}C_T \sin\gamma}{\theta_{c_0}(1-2a)}\right)}}. \tag{35}$$

The non-deflection-side width has no closed-form counterpart (Eq. (A11)), but over $0.2 \le C_T \le 0.95$ it stays within about $10\,\%$ of $2\sigma_\ell$, whereas τ_{A_ℓ} falls by as much as $43\,\%$, from $0.97\sigma_\ell$ to $0.56\sigma_\ell$ at $\gamma = 30°$ (Fig. A2). We therefore fix $\tau_{B_\ell} = 2\sigma_\ell$ and evaluate τ_{A_ℓ} for each turbine from Eq. (35), which keeps the model non-iterative while retaining the C_T dependence where it matters for the deflection. At zero yaw, Eq. (35) is indeterminate, and we take $\tau_{A_\ell} = 0.75\sigma_\ell$. Assuming further that τ_B grows at the same rate as the streamwise wake, $k_{V_B} = k_U$, and that the ratio τ_A/τ_B is independent of downstream distance,

$$k_{V_A} = \frac{\tau_{A_\ell}}{\tau_{B_\ell}} k_{V_B} = \frac{\tau_{A_\ell}}{\tau_{B_\ell}} k_U = \frac{\tau_{A_\ell}}{2\sigma_\ell} k_U, \tag{36}$$

so that k_{V_A} varies with C_T rather than taking a single fixed value; it recovers $k_{V_A} = \frac{3}{8}k_U$ at $C_T \approx 0.72$, where $\tau_{A_\ell} \approx 0.75\sigma_\ell$.

Table 1 collects the modelling assumptions and closure constants introduced above, with the equation or figure that justifies each, and Algorithm B1 in App. B gives implementation-oriented pseudocode; together they are intended to allow the model to be implemented without recourse to the derivation. Rotor averages use the 21-point circular Gauss quadrature of PyWake (Pedersen et al., 2023). The results presented here use a streamwise step of $\Delta x = D/32$. Because the deflection is obtained by explicit Euler integration of the local skew angle, it converges at first order in Δx, and at this step the residual error in the far-wake deflection is below $5 \times 10^{-4} D$. The deflection solve for a three-turbine case takes approximately $0.2\,\mathrm{s}$ single-threaded in the reference Python implementation; constructing the three-dimensional velocity field, here at $\Delta y = D/256$ and $\Delta z = z_h/5$, is a separate step required only for the figures.

4 Model predictions

This section compares the model with wind-tunnel measurements, which tests its behaviour rather than constituting a comprehensive validation (proposed as further work in Sect. 5). Section 4.1 first reviews single-turbine cases. Section 4.2 then forms the core of the results: Sect. 4.2.1 examines the interaction mechanisms, and the decomposition of the resulting deflections, through the streamwise and lateral velocity fields that the model provides; Sect. 4.2.2 compares the predicted wake-centre deflection against PIV data and established engineering models; and Sect. 4.2.3 extends the comparison to the full hub-height velocity field, which ultimately sets the inflow, and hence the available power, of each downstream turbine.

4.1 Single-turbine validation

We begin with the single-turbine experiments of Bastankhah and Porté-Agel (2016, Sect. 2), in which a turbine was operated at an inflow velocity of $4.88\,\mathrm{m\,s^{-1}}$ and a turbulence intensity of $7.7\,\%$, and velocity fields were measured using planar particle

https://doi.org/10.5194/wes-2026-183
Preprint. Discussion started: 4 November 2026
© Author(s) 2026. CC BY 4.0 License.

eawe european academy of wind energy
Open Access WIND ENERGY SCIENCE DISCUSSIONS

Table 1. Summary of the modelling assumptions and closure constants used in the present model. Numerical scheme choices (deflection integration, rotor-averaging discretisation) are described in the text and Algorithm B1.

Assumption / constant	**Value or expression**	**Basis**
Momentum-deficit coefficient	$\alpha = 2$	Exact solution of Eq. (2); cf. $\alpha = 1$ in Bastankhah et al. (2021)
Wake profiles	Streamwise: symmetric Gaussian, Eq. (9); lateral: asymmetric Gaussian, Eq. (16), negative velocities neglected	Self-similarity, Fig. 2(a) and (b)
Thrust coefficient	$C_{T,i} = 0.82\cos^{1.8}\gamma_i$	Eq. (12) from Zong and Porté-Agel (2021)
Near-wake peak velocities	$\Delta\tilde{U}_{\mathrm{nw}}/U_h = 2a\langle U\rangle/U_h$, $\Delta\tilde{V}_{\mathrm{nw}}/U_h = -\frac{1}{4}C_T(\langle U\rangle/U_h)\sin\gamma$; Eqs. (27)–(25)	Shapiro et al. (2018)
Near-/far-wake switch	Magnitude criterion χ, Eq. (28): near-wake values retained while the far-wake self-deficit exceeds the near-wake value; upstream contributions ($\Delta\tilde{U}^{\mathrm{int}}$, $\Delta\tilde{V}^{\mathrm{inh}}$) suppressed in the active near wake	Near wake governed by local turbine dynamics (Crespo et al., 1999; Lignarolo et al., 2014)
Potential-core length x_0	Eq. (A3); $\alpha^* = 2.32$, $\beta^* = 0.154$; positions the width line only	Bastankhah and Porté-Agel (2016)
Widths at end of potential core	Eq. (A1); geometric mean $\sigma_0 = \sqrt{\sigma_{y_0}\sigma_{z_0}}$, Eq. (A2)	Bastankhah and Porté-Agel (2016)
Far-wake onset ℓ	Where χ turns off: width σ_ℓ, Eq. (A4); distance ℓ, Eq. (A5); anchors the lateral onset widths and their growth	Continuity of $\Delta\tilde{U}$ between Eqs. (10) and (25)
Streamwise growth rate k_U	$k_U = 0.38\,I_{\mathrm{local}} + 0.004$; $I_{\mathrm{local},i} = \sqrt{I_0^2 + \max_j \Delta I_{ij}^2}$	Niayifar and Porté-Agel (2016)
Added turbulence ΔI	$\Delta I = 0.9\,a^{0.8325} I_0^{-0.0325}(\Delta x/D)^{-0.56}$, weighted by the rotor–wake overlap fraction; maximum over upstream turbines	Turbulence-optimised Crespo and Hernández (1996); Eqs. (7)–(8) of Zehtabiyan-Rezaie et al. (2024)
Skew angle at far-wake onset	$\theta_\ell = \theta_{c_0} = \dfrac{0.3\gamma}{\cos\gamma}\left(1 - \sqrt{1 - C_T\cos\gamma}\right)$	Eq. (6.12) from Bastankhah and Porté-Agel (2016); constant across the potential core, taken at the onset (Eq. (A5))
Lateral onset widths	$\tau_{A\ell}$ from Eq. (35) (closed form; $0.75\,\sigma_\ell$ at $\gamma = 0$), $\tau_{B\ell} = 2\,\sigma_\ell$	$\tau_{B\ell}$ fixed at $2\sigma_\ell$, motivated by Eq. (A11) and Fig. A2(b)
Lateral growth rates	$k_{V_B} = k_U$, $\quad k_{V_A} = (\tau_{A\ell}/\tau_{B\ell})\,k_U$	Eq. (36)
Near-wake lateral widths	$\tau_{A\phi} = (\tau_{A\ell}/\sigma_\ell)\,\sigma_\phi$, $\quad \tau_{B\phi} = 2\,\sigma_\phi$	Continuity to onset values; Algorithm B1
Lateral wake centre	$\epsilon_i/D = (\delta_i - s_i\,\sigma_i)/D$, deflection-side sign s_i of Eq. (17)	Eq. (32); small-angle approximation $V \ll U$
Inflow lateral velocity	$V_0 = 0$	Coordinate system aligned with hub-height inflow

https://doi.org/10.5194/wes-2026-183
Preprint. Discussion started: 4 November 2026
© Author(s) 2026. CC BY 4.0 License.

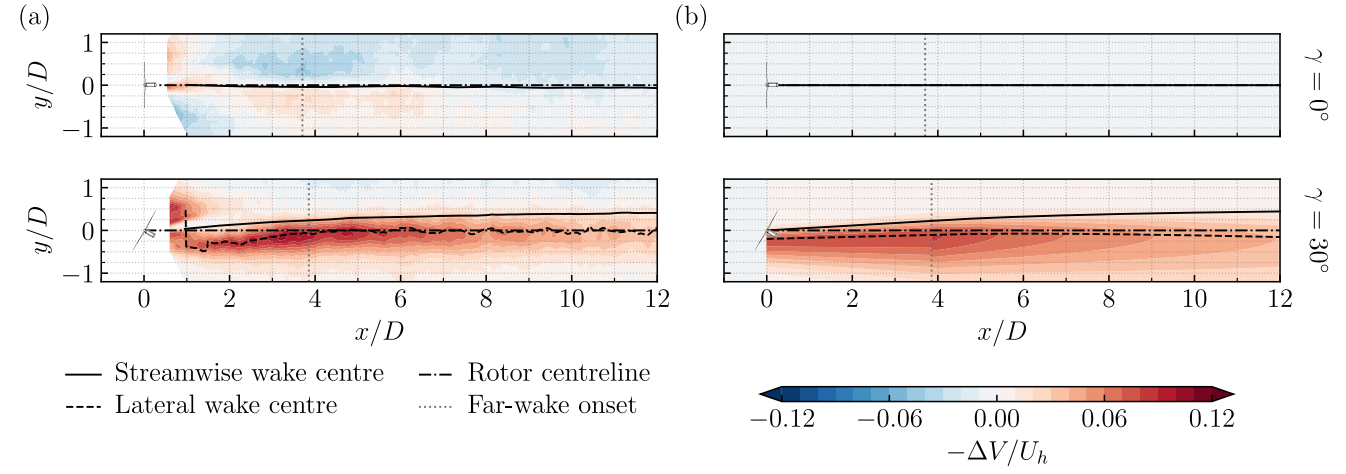

Figure 4. Contours of normalised lateral velocity surplus ($-\Delta V/U_h$) in the horizontal plane at hub height for yaw angles of 0° and 30° (labelled in each subplot). Column (a) shows planar PIV measurements from Bastankhah and Porté-Agel (2016); column (b) shows results from the present model configured to replicate the same experimental setup. The far-wake onset is given by Eq. (28).

image velocimetry (PIV) at yaw angles of 0°, 10°, 20° and 30°. The figures show 0° and 30°; the errors quoted cover all four. The measured incoming boundary-layer profile of Bastankhah and Porté-Agel (2016, Fig. 1) is imposed as the inflow, fitted to a logarithmic law and shifted so that the hub-height speed is exactly U_h. The shear lowers the rotor-averaged incoming velocity of Eq. (3) to $\langle U \rangle = 0.991\,U_h$, which rescales the thrust and the near-wake amplitudes and changes the predicted deflection by less than $0.01D$. The thrust coefficient is $C_T = 0.82\cos^{1.8}\gamma$ (Zong and Porté-Agel, 2021, Eq. 12), giving $C_T = 0.82$, 0.80, 0.73 and 0.63 at the four yaw angles, with induction factors $a = 0.29$, 0.28, 0.24 and 0.20 from Eq. (26).

The model predicts the lateral velocity as part of the solution, and the deflection follows from it through the skew angle. Figure 4 compares the lateral velocity with the PIV, whose lateral wake centre (dashed line) is found by fitting an asymmetric Gaussian at each downstream station. The lateral velocities are at least an order of magnitude smaller than the streamwise velocities, and the lateral wake is less sharply defined, but in the far wake, the model reproduces its magnitude, centre, and shape, as well as the growth of the lateral velocity with yaw angle. Along the streamwise wake centre (solid line), where the deflection is evaluated, the prediction is consistent with the measurements.

Figure 5 extracts both velocity components along the measured streamwise wake centre. In the far wake, the model agrees closely with the streamwise velocity and, allowing for the noisier measurement, with the lateral velocity. In the near wake, the solutions of Eqs. (25) and (27) are an oversimplification: the streamwise deficit is significantly underpredicted. The small step in the lateral velocity at the onset comes from the near-wake switch, Eq. (28), a limitation taken up in Sect. 5.

Figure 6 compares the predicted wake centrelines with the measured ones – found by fitting a Gaussian to the streamwise deficit profile of the PIV at each downstream station – and with the models of Bastankhah and Porté-Agel (2016, Eq. (7.4)) and Jiménez et al. (2010). The Jiménez et al. (2010) model is PyWake v2.6.19's `JimenezWakeDeflection` (Pedersen et al.,

https://doi.org/10.5194/wes-2026-183
Preprint. Discussion started: 4 November 2026
© Author(s) 2026. CC BY 4.0 License.

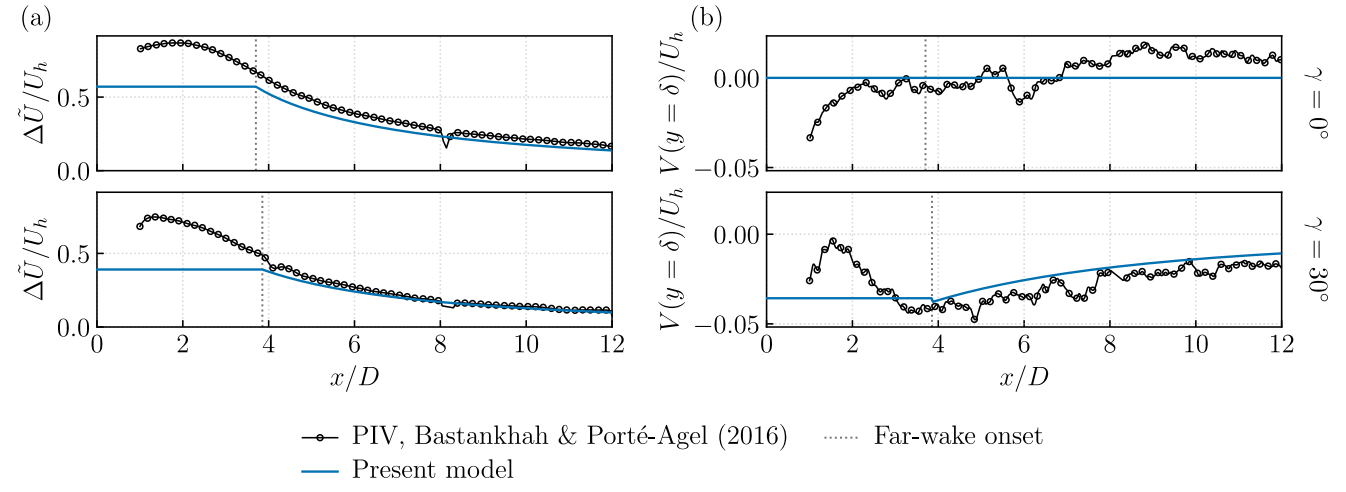

Figure 5. Normalised (a) streamwise velocity deficit and (b) lateral velocity along the streamwise wake centreline at hub height for yaw angles of 0° and 30° (labelled in each subplot), compared against planar PIV measurements of Bastankhah and Porté-Agel (2016). The streamwise wake centreline is found by fitting a symmetric Gaussian to the streamwise deficit profile, and the far-wake onset is given by Eq. (28).

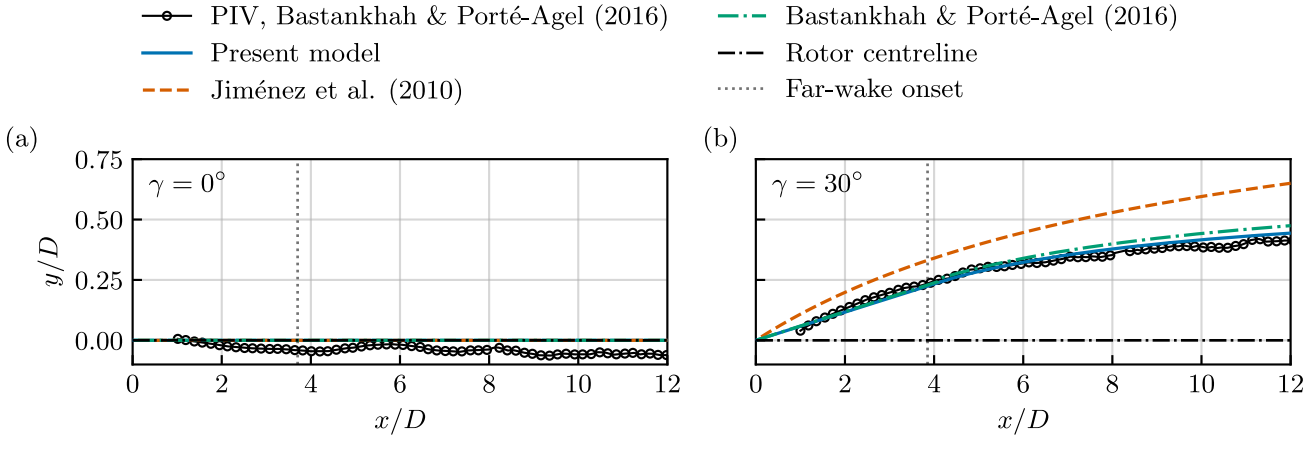

Figure 6. Streamwise wake centreline location in the horizontal (x–y) plane at hub height for a single turbine at (a) $\gamma_1 = 0°$ and (b) $\gamma_1 = 30°$, compared against planar PIV measurements by Bastankhah and Porté-Agel (2016) and predictions from the models of Bastankhah and Porté-Agel (2016) and Jiménez et al. (2010). The far-wake onset for each turbine is given by Eq. (28).

https://doi.org/10.5194/wes-2026-183
Preprint. Discussion started: 4 November 2026
© Author(s) 2026. CC BY 4.0 License.

eawe european academy of wind energy
Open Access WIND ENERGY SCIENCE DISCUSSIONS

Table 2. Overview of multi-turbine test cases used in Sect. 4.2.

Case	Turbine positions $(x/D,\ y/D)$	Yaw angles (°)
Case A_0	$(0,0)$, $(5,0)$, $(10,0)$	$0, 0, 0$
Case A_1	$(0,0)$, $(5,0)$, $(10,0)$	$-30, 0, 0$
Case A_2	$(0,0)$, $(5,0)$, $(10,0)$	$-30, -20, 0$
Case A_3	$(0,0)$, $(5,0)$, $(10,0)$	$-25, -15, 0$
Case A_4	$(0,0)$, $(5,0)$, $(10,0)$	$25, 20, 0$
Case S_0	$(0,0)$, $(5,\frac{1}{3})$, $(10,\frac{2}{3})$	$0, 0, 0$
Case S_1	$(0,0)$, $(5,\frac{1}{3})$, $(10,\frac{2}{3})$	$-20, -20, 0$

2023) in its standard and most widely used form, with a fixed wake-spreading rate $\beta = 0.1$; tying β to the local turbulence intensity instead roughly doubles its single-turbine far-wake error (App. C), so the standard form is the stronger baseline. The present model and that of Bastankhah and Porté-Agel (2016) agree closely, as expected of two models that fit Gaussians to predict the skew angle, and both compare well with the measured far-wake deflection, least closely at $10°$ and $20°$; the Jiménez model overpredicts it at every yaw angle, as reported previously (Porté-Agel et al., 2020). Averaged over the yawed cases ($10°$–$30°$), the far-wake RMSE is $0.037D$, $0.059D$ and $0.198D$ respectively (Fig. 11). The present model thus performs on par with existing momentum-based approaches for a single turbine, and we turn to the multi-turbine cases.

4.2 Multi-turbine interaction

The three-turbine cases are those of Zong and Porté-Agel (2020, 2021), in which one or more of the first two turbines were yawed and hub-height velocity fields were measured using planar PIV. An overview is provided in Table 2: five aligned configurations (denoted A_0–A_4) and two staggered layouts (denoted S_0 and S_1), which encompass examples of strong secondary wake steering (King et al., 2021), yawed wake superposition, partial wake overlap, and both negative and positive yaw angles. Thrust coefficients for the turbines are calculated as $0.82\,(\cos\gamma_i)^{1.8}$ (Zong and Porté-Agel, 2021, Eq. (12)). The cases are run with uniform inflow: Zong and Porté-Agel (2020, 2021) report no parameterisation of the incoming boundary-layer profile and themselves take the hub-height velocity as the reference velocity, so we adopt the same assumption rather than impose an inflow condition of our own construction.

The Jiménez et al. (2010) model provides only a deflection law, so to predict a velocity field, it must be embedded in a complete wake model. We embed it in PyWake with the closures the present model uses, with the same coefficients: a Gaussian deficit whose expansion rate is the k_U of Eq. (31), the same added-turbulence model, and the same thrust coefficient; the wakes are combined by linear superposition of the individual deficits. Matching the closures isolates the deflection and wake-interaction physics that distinguish the two models. Two consequences follow. Firstly, the label "Jiménez et al. (2010)" is used throughout for this composite, of which only the deflection law is due to that reference. Secondly, the wake centrelines

https://doi.org/10.5194/wes-2026-183
Preprint. Discussion started: 4 November 2026
© Author(s) 2026. CC BY 4.0 License.

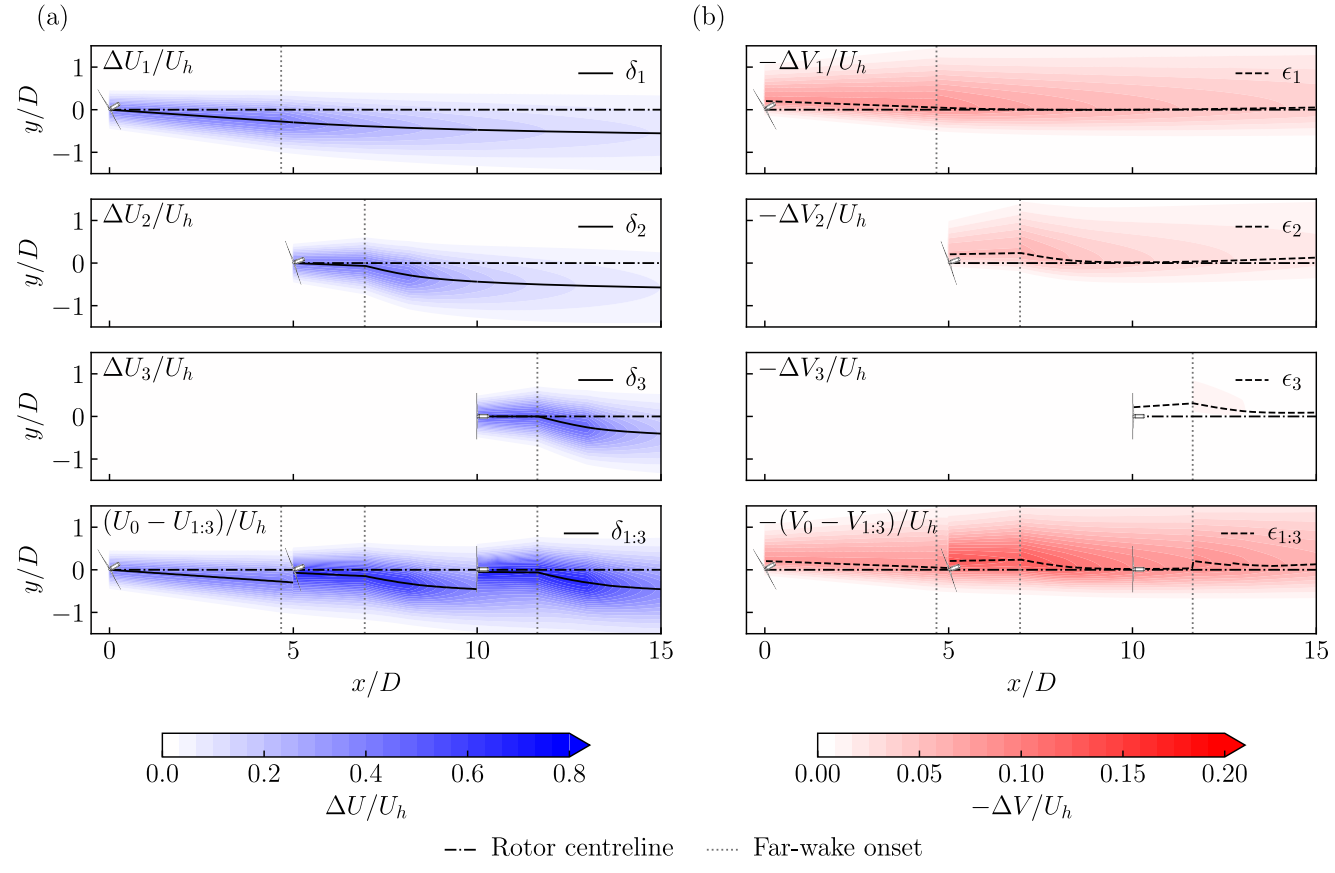

Figure 7. Cumulative streamwise deficit and lateral surplus fields in the horizontal (x–y) plane at hub height for the aligned three-turbine configuration of Case A_2 ($\gamma_1 = -30°$, $\gamma_2 = -20°$, $\gamma_3 = 0°$; see Table 2), decomposed by turbine. Contours in (a) depict the streamwise velocity deficits $(U_{i-1} - U_i)/U_h$; contours in (b) show the lateral velocity surpluses $-(V_{i-1} - V_i)/U_h$, as defined in Eq. (6). The bottom panels present the cumulative fields, $(U_0 - U_{1:3})/U_h$ and $-(V_0 - V_{1:3})/U_h$. The far-wake onset for each turbine is given by Eq. (28).

of Sect. 4.2.2 are fitted to the composite velocity field, so they depend on the deficit and superposition models as well as on the deflection law, particularly where wakes merge. Appendix C tests the sensitivity of the comparison to the superposition rule.

4.2.1 Physical insight

Figure 7 decomposes the field of Case A_2 by turbine. In the top row, the wake of WT_1 ($\gamma_1 = -30°$) is deflected towards negative y by the ratio of its lateral to its streamwise velocity at δ_1, as for the single turbine of Sect. 4.1.

The second row shows $\Delta\tilde{U}_2 f_2$ and $-\Delta\tilde{V}_2 g_2$ for WT_2 ($\gamma_2 = -20°$), whose lateral surplus has a thrust-driven and an inherited component (Eqs. (21) and (22)). In the near wake the amplitudes are those of the turbine alone, capped by Eqs. (25) and (27), so there $\Delta\tilde{V}_2 = \Delta\tilde{V}_2^{\mathrm{thr}}$; the upstream wakes enter only in the far wake. The effect is clearest in the third row: WT_3 is unyawed,

https://doi.org/10.5194/wes-2026-183
Preprint. Discussion started: 4 November 2026
© Author(s) 2026. CC BY 4.0 License.

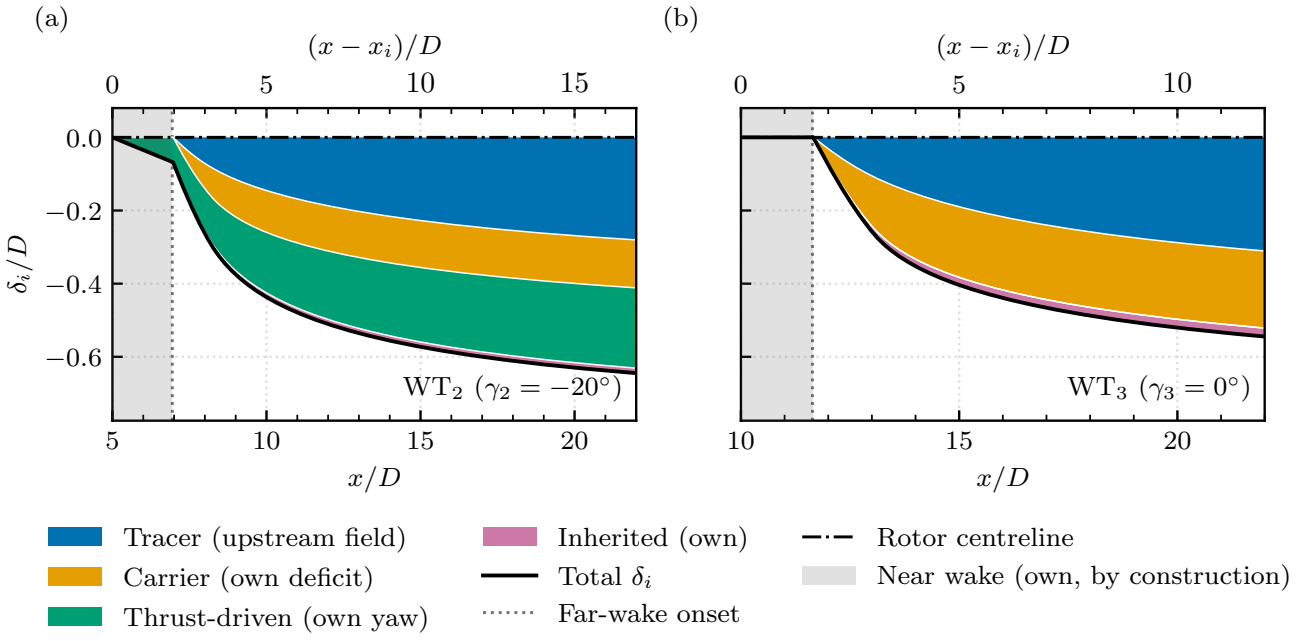

Figure 8. Decomposition of the wake-centre deflection δ_i of (a) WT$_2$ ($\gamma_2 = -20°$) and (b) WT$_3$ ($\gamma_3 = 0°$) in Case A$_2$ into the tracer, carrier, thrust-driven and inherited components of Eq. (30), stacked from $\delta_i = 0$; they sum to the total (solid black line) exactly. The shaded strip is the near wake, upstream of the far-wake onset of Eq. (28) (dotted), where the deflection is thrust-driven by construction. The upper axis shows the downstream distance from each turbine's rotor.

so has no thrust-driven component, yet its far wake carries lateral velocity, all of it inherited, and is visibly deflected. The advected lateral velocity of WT$_1$ and WT$_2$ appears separately, in the cumulative panel.

Figure 8 integrates the four components of Eq. (30) along x. The shares below are of δ_i at the end of the domain ($x = 22D$), not of θ_i at any one station, and the parts due to the rotor's presence are front-loaded: just downstream of the far-wake onset, the skew angle of the unyawed WT$_3$ is 2.4 times the tracer's, but $8D$ behind the rotor only 13 % steeper. The shares drift accordingly: $4D$ behind each unyawed downstream rotor the carrier still outweighs the tracer (48–52 against 43–47 %), whereas at the end of the domain the tracer leads. The near wake, thrust-driven by construction (Sect. 3), contributes 10.4 % of δ_2. The shares attribute the computed deflection; they are not the change that removing a term would cause.

For the unyawed WT$_3$, the tracer accounts for 57.0 % of the deflection, the carrier for 38.7 % and the inherited lateral velocity for 4.2 %: of the 42.9 % due to the rotor's own presence, almost all is its streamwise deficit amplifying the upstream cross-flow, and only 4.2 % the lateral velocity its own wake carries. Every unyawed downstream rotor in Cases A$_1$–A$_3$ and S$_1$ behaves alike (57–66, 31–39 and 3.5–4.2 %). For the yawed WT$_2$, the four shares are 43.5, 20.3, 34.1 and 2.1 %, so the upstream wake still contributes more than the turbine's own yaw. The inherited part is small throughout; its significance is that it is the one component the linearised balance of Sect. 2 loses. A superposition of prescribed deflections has neither a cross-flow

https://doi.org/10.5194/wes-2026-183
Preprint. Discussion started: 4 November 2026
© Author(s) 2026. CC BY 4.0 License.

for a downstream wake to be advected by nor a slower wake for that cross-flow to act on, nor an inherited lateral velocity, and so represents only the thrust part.

4.2.2 Streamwise wake deflection

Figures 9 and 10 compare the predicted wake-centre trajectories for the cases of Table 2 with the PIV measurements of Zong and Porté-Agel (2020, 2021), together with the model of Jiménez et al. (2010) and, where a published curve is available, that of Zong and Porté-Agel (2020), with a focus on how well each captures wake interactions and secondary wake steering.

Wake centrelines are extracted in the same way for all models and datasets: a Gaussian is fitted to the hub-height streamwise deficit at each downstream station, and its centre is taken; the full procedure is given in the accompanying code. As the wake centre is not uniquely defined, this standardisation ensures that the comparison reflects differences between the predicted and measured fields rather than between centreline definitions. One consequence is that the centrelines extracted here from the PIV of Bastankhah and Porté-Agel (2016) and Zong and Porté-Agel (2020, 2021) differ from those reported in the original references, although the underlying velocity fields are the same. Figure 11 reduces each case to a single accuracy measure, the root-mean-square error (RMSE) of the far-wake deflection (δ/D) relative to the experimental reference, evaluated at the PIV measurement points beyond the far-wake onset.

The two zero-yaw cases, A_0 and S_0, confirm that the deflections seen elsewhere are physical rather than artefacts of the model or the reference data. In Case A_0, the present model and that of Jiménez et al. (2010) both predict zero deflection throughout the domain, and the PIV centreline remains within roughly $0.05D$ of $y = 0$ in the far wake, so the aligned inflow is effectively symmetrical. In Case S_0, no turbine is yawed, yet the measured centreline drifts laterally downstream. Two mechanisms can produce this drift. The laterally offset wakes superpose asymmetrically, and Zong and Porté-Agel (2021) attribute part of the drift to the uneven recovery of the two sides of the downstream wake under the lateral shear of the partial-wake inflow. Both models represent only the first, through their cumulative fields, and both reproduce a drift of the observed sign and order, which shows that superposition alone suffices; the agreement may nonetheless absorb a contribution from the second, which neither model resolves. Of the two, the present model is the closer (Fig. 11).

Across the yawed configurations, the model reproduces the deflection of the directly yawed wakes well. The principal discrepancy is an underprediction of the near wake, most evident for WT_2 in Cases A_4 and S_1, which a steep far-wake deflection often corrects; with a more accurate near-wake model, this could lead to an overprediction of the deflection.

The leading wakes of Cases A_1 and A_2 raise a question that Fig. 6 anticipates: the Jiménez et al. (2010) baseline, which markedly overpredicts the single-turbine deflection, agrees closely with them. Two differences in the comparison account for this. The leading wake can be compared only up to WT_2 at $5D$, before the overprediction has grown ($+0.078D$ rather than $+0.141D$ at 30°), and the leading turbine of Zong and Porté-Agel (2020) deflects some $15\,\%$ more than that of Bastankhah and Porté-Agel (2016), consistent with the lower ambient turbulence intensity of the three-turbine experiment ($6.0\,\%$ against $7.7\,\%$). The agreement is thus specific to these conditions (App. C).

The defining capability of the model is that it produces secondary wake steering mechanistically, through the momentum-conserving velocity field (Sect. 4.2.1), rather than through deflection superposition alone. Case A_1 is the cleanest demonstra-

https://doi.org/10.5194/wes-2026-183
Preprint. Discussion started: 4 November 2026
© Author(s) 2026. CC BY 4.0 License.

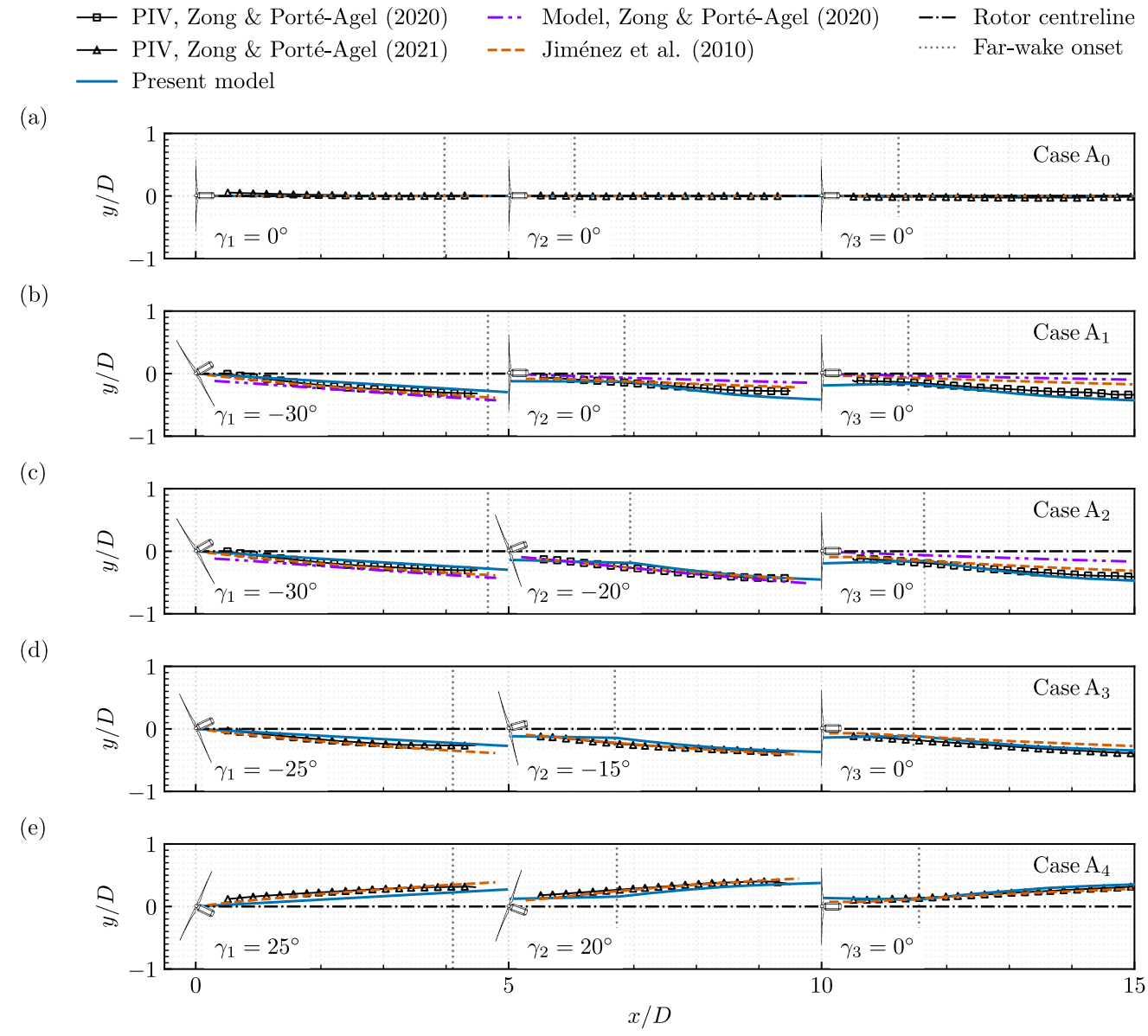

Figure 9. Streamwise wake centreline location in the horizontal (x–y) plane at hub height for the aligned configuration of three turbines spaced $5D$ apart. The schematics denote the rotor footprints with their corresponding yaw angles for (a) Case A_0, (b) Case A_1, (c) Case A_2, (d) Case A_3, and (e) Case A_4, as defined in Table 2, compared against PIV measurements by Zong and Porté-Agel (2020, 2021) and predictions from the model of Jiménez et al. (2010), together with that of Zong and Porté-Agel (2020) where a published curve is available (panels (b) and (c)). The far-wake onset for each turbine is given by Eq. (28). Predictions labelled Jiménez et al. (2010) are those of the composite baseline defined in Sect. 4.2 and Appendix C, of which only the deflection law is due to that reference.

https://doi.org/10.5194/wes-2026-183
Preprint. Discussion started: 4 November 2026
© Author(s) 2026. CC BY 4.0 License.

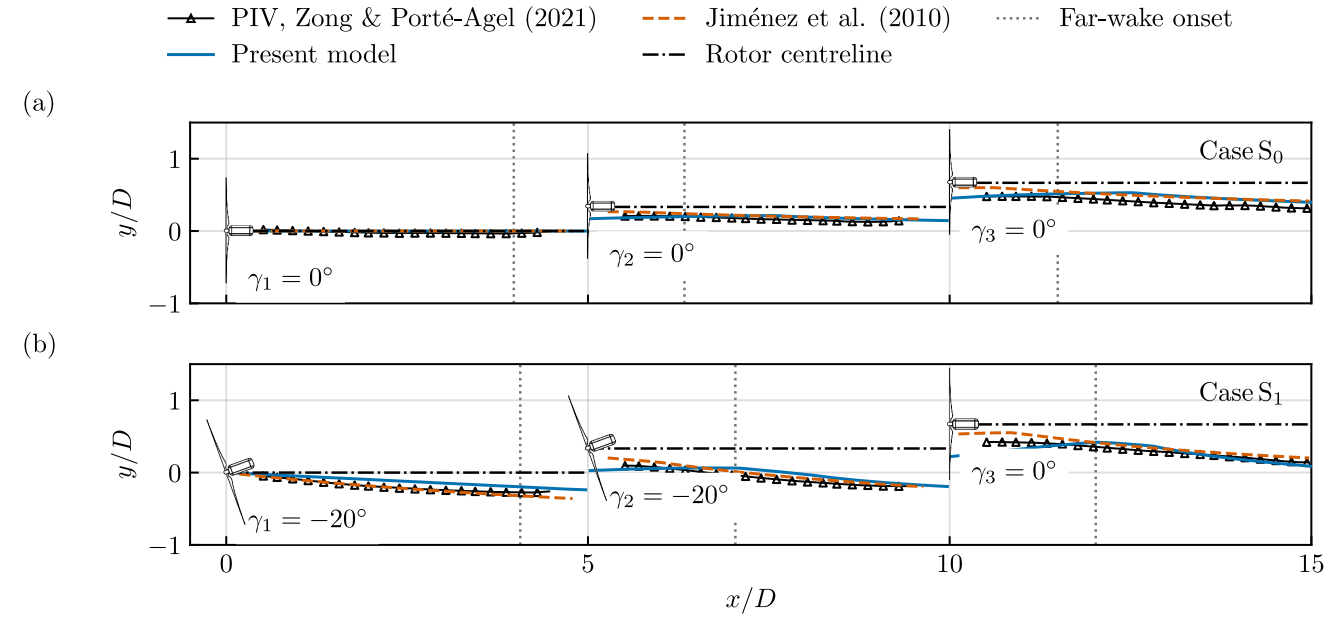

Figure 10. Streamwise wake centreline location in the horizontal (x–y) plane at hub height for the staggered configuration of three turbines spaced $5D$ apart. Schematics denote the rotor footprints with their corresponding yaw angles for (a) Case S_0, and (b) Case S_1, as defined in Table 2, compared against planar PIV measurements by Zong and Porté-Agel (2021) and predictions from Jiménez et al. (2010). The far-wake onset for each turbine is given by Eq. (28).

tion. Only the upstream rotor is yawed, so the wakes of WT_2 and WT_3 carry no thrust-driven lateral velocity; nonetheless, the measured centreline behind WT_3 departs markedly from $y = 0$, a clear case of secondary wake steering. The present model captures this. The model of Jiménez et al. (2010) contains no secondary-steering physics, so its downstream displacement results solely from the advection of the upstream yawed wake, which it over-deflects (Qian and Ishihara, 2018; Brugger et al., 2020); where it agrees with the data, it does so for the wrong reason. The residuals show this. In A_1 the present model has the lower error (0.060 against 0.098), and behind the unyawed turbines it slightly overpredicts the deflection, whereas Jiménez et al. (2010), although it over-deflects the yawed leading wake, underpredicts it there, as nothing in it deflects an unyawed wake. The model of Zong and Porté-Agel (2020) does include a secondary-steering mechanism, but it appears to underestimate its strength (Cases A_1 and A_2). The cumulative curl model (Bay et al., 2023) also produces secondary steering, but through an effective yaw angle rather than a solved lateral velocity (Sect. 1); comparing the two on these cases is left to future work.

The staggered cases prove the most difficult, particularly Case S_1, for two reasons. Where offset wakes overlap, their deficit profiles depart from a single Gaussian, so the fitted centreline is least reliable there, for both the modelled and the measured fields (Vollmer et al., 2016). Moreover, the asymmetric Gaussian is least accurate on the flanks of the lateral wake (Fig. 2(b)), and the staggered layout places each successive rotor a further $D/3$ out on the flank of the upstream wakes, from where it draws the advected lateral velocity that, with the carrier effect it drives, sets most of its deflection (Fig. 8). For S_1, the present

https://doi.org/10.5194/wes-2026-183
Preprint. Discussion started: 4 November 2026
© Author(s) 2026. CC BY 4.0 License.

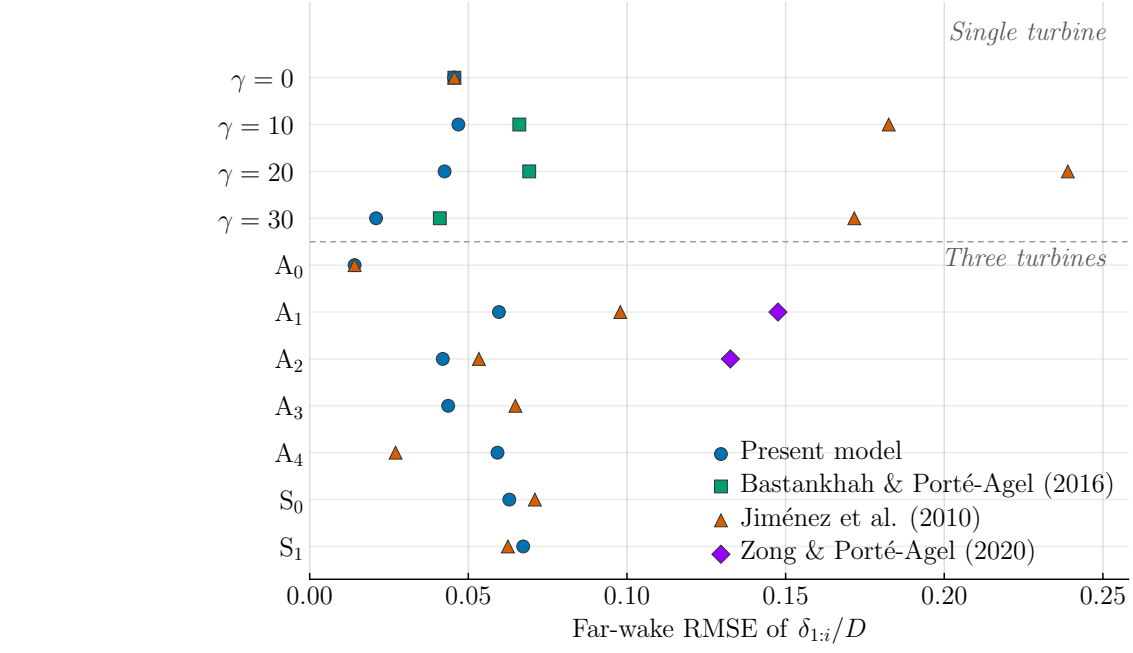

Figure 11. Per-case accuracy of the predicted wake-centre deflection. Each marker shows the root-mean-square error (RMSE) of the far-wake centreline deflection δ/D for one model relative to the experimental reference (lower is better; see legend for the models). Single-turbine cases ($\gamma = 0°, 10°, 20°, 30°$) are compared with the Bastankhah and Porté-Agel (2016) PIV measurements; three-turbine cases (aligned A_0–A_4, staggered S_0–S_1) with the deflection reported by Zong and Porté-Agel (2020, 2021). The wake centre is taken as the centre of a fitted Gaussian, and the error is evaluated over the far-wake region (downstream of the far-wake onset) at the experimental measurement stations.

model is the weaker of the two (0.067 against 0.062); Sect. 4.2.3 returns to this case with a measure that requires no centreline. Across the three-turbine configurations, the present model attains the lower far-wake error in A_1, A_2, A_3 and S_0, the unyawed A_0 is a tie, and Jiménez et al. (2010) is closer in A_4 and, marginally, S_1 (Fig. 11).

4.2.3 Streamwise velocity field

The deflection comparison isolates wake steering, but the model exists to predict the velocity field that sets the inflow, and with it the power, of each downstream turbine. A velocity-field comparison also requires no wake centre, so it remains well defined where the centreline becomes ambiguous. Because both models are evaluated at the same measurement points and share their closures, their residuals differ only in the deflection and interaction physics and in how the wakes are combined.

Figure 12 reduces each case to the RMSE of U/U_h over the hub-height plane resolved by the PIV, evaluated over the far-wake region and computed identically for both models at the same measurement points, mirroring Fig. 11. The present model attains the lower field error in every three-turbine case, where the deflection comparison did not clearly separate the two; averaged over the seven cases, its far-wake field RMSE is $0.050\,U_h$, against $0.087\,U_h$ for the model of Jiménez et al. (2010).

https://doi.org/10.5194/wes-2026-183
Preprint. Discussion started: 4 November 2026
© Author(s) 2026. CC BY 4.0 License.

eawe european academy of wind energy
Open Access WIND ENERGY SCIENCE DISCUSSIONS

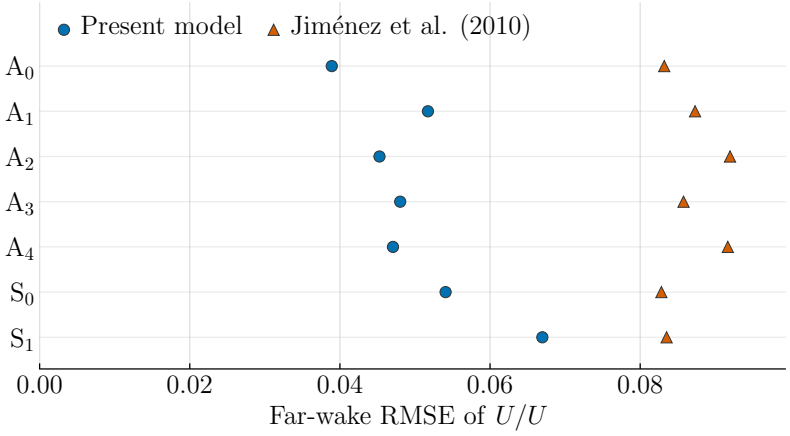

Figure 12. Per-case accuracy of the predicted hub-height streamwise velocity field. Each marker shows the root-mean-square error (RMSE) of the normalised velocity U/U_h over the whole hub-height plane resolved by the PIV (common domain $0 \leq x/D \leq 15$, $|y|/D \leq 2$), evaluated over the far-wake region, for the present model and Jiménez et al. (2010) against the measurements of Zong and Porté-Agel (2020, 2021). In contrast to the centreline deflection, the present model attains the lower field error in every case.

Because the baseline is a composite, the margin could depend on how it combines its wakes – the one component that the baseline chooses and the present model derives. Replacing the linear superposition in turn by three alternatives (Appendix C, Table C1) leaves the ranking unchanged but for one case: the present model attains the lower error everywhere except Case S_1 under the momentum-conserving rule, where the two are a dead heat (0.0670 against $0.0667\,U_h$). The baseline's mean error ranges from 0.064 to $0.087\,U_h$ across the variants, so the size of the margin is a property of the composite, but its sign is not.

Figures 13 and 14 show where the two models depart from the measurement. The residuals differ in character. Close behind each rotor, that of the present model is large and positive: as for the single turbine (Sect. 4.1), the near-wake deficit is underpredicted. Beyond the far-wake onset it is small and smooth, a mild positive difference along the wakes: the modelled velocity is slightly too high, and the deficit correspondingly underpredicted. Over the far-wake region this bias reaches $+0.026\,U_h$ in Case S_1 and stays below $+0.006\,U_h$ in the aligned cases. The small positive bias is the field-level counterpart of the near-wake behaviour of Sect. 4.2.2: an underpredicted streamwise deficit raises the local velocity, which lowers the skew angle and hence the integrated deflection, so one modest error accounts for both the near-wake deflection and the field bias rather than two independent shortcomings.

The residual of Jiménez et al. (2010) is larger and has two components: a net negative offset, corresponding to an overpredicted deficit and strongest in the near wakes, and a lateral dipole with opposite signs on the two flanks of each wake, as a wake displaced to one side of the measured one produces. The offset is a property of the linear superposition of ambient-scaled deficits and changes sign under squared summation, as the variants of Appendix C show.

Two caveats bound this interpretation, neither of which affects the ranking. Firstly, the field RMSE reflects the magnitude of the deficit as much as the steering, so it complements the deflection comparison rather than replacing it. Secondly, neither model reproduces the near-rotor speed-up, so clipping the PIV at $U/U_h = 1$ affects them equally.

https://doi.org/10.5194/wes-2026-183
Preprint. Discussion started: 4 November 2026
© Author(s) 2026. CC BY 4.0 License.

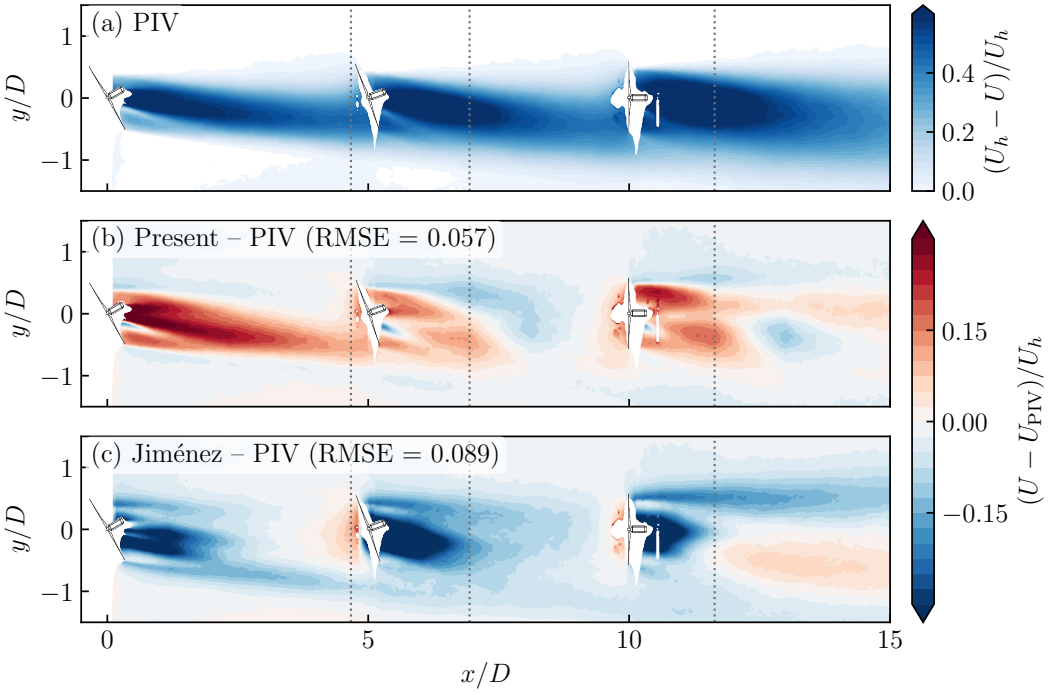

Figure 13. Hub-height streamwise velocity field for the aligned Case A_2 ($\gamma_1 = -30°$, $\gamma_2 = -20°$, $\gamma_3 = 0°$): (a) the measured PIV deficit $(U_h - U)/U_h$; (b) present model minus PIV; (c) Jiménez et al. (2010) minus PIV. In the difference panels, positive (red) means the model is faster than the measurement, i.e. it underpredicts the deficit, and negative (blue) that it overpredicts it; the diverging scale saturates at $\pm 0.3 U_h$. Rotor schematics show the yaw angles and the dotted lines the far-wake onsets. Beyond the far-wake onsets, the present model's residual is small and smooth, with an under-deficit, whereas the Jiménez et al. (2010) residual is larger and exhibits a lateral dipole at each wake, where its wakes are displaced from the measured ones.

5 Summary and future research

In this study, the momentum-conserving framework of Bastankhah et al. (2021) was extended to an analytical wake-steering model for wind farms, based on the approximate conservation of the momentum deficit in both the streamwise and lateral direction. By coupling the streamwise and lateral dynamics into a single analytical framework, the model derives the lateral velocity field and diagnostically predicts wake deflection by integrating the local skew angle, thereby requiring neither effective yaw angles nor iterative solution procedures.

A key feature of the framework is the distinction between the streamwise and lateral wakes, which allows the model to represent the spatial distribution of lateral momentum induced by yaw misalignment. Secondary wake steering then emerges from the governing equations, without empirical correction factors, through three routes: the cross-flow of yawed upstream turbines advects each downstream wake; the downstream turbine's own streamwise deficit slows the flow carrying that cross-flow, and so amplifies it; and the turbine's lateral wake inherits lateral momentum from the upstream flow, even when the

https://doi.org/10.5194/wes-2026-183
Preprint. Discussion started: 4 November 2026
© Author(s) 2026. CC BY 4.0 License.

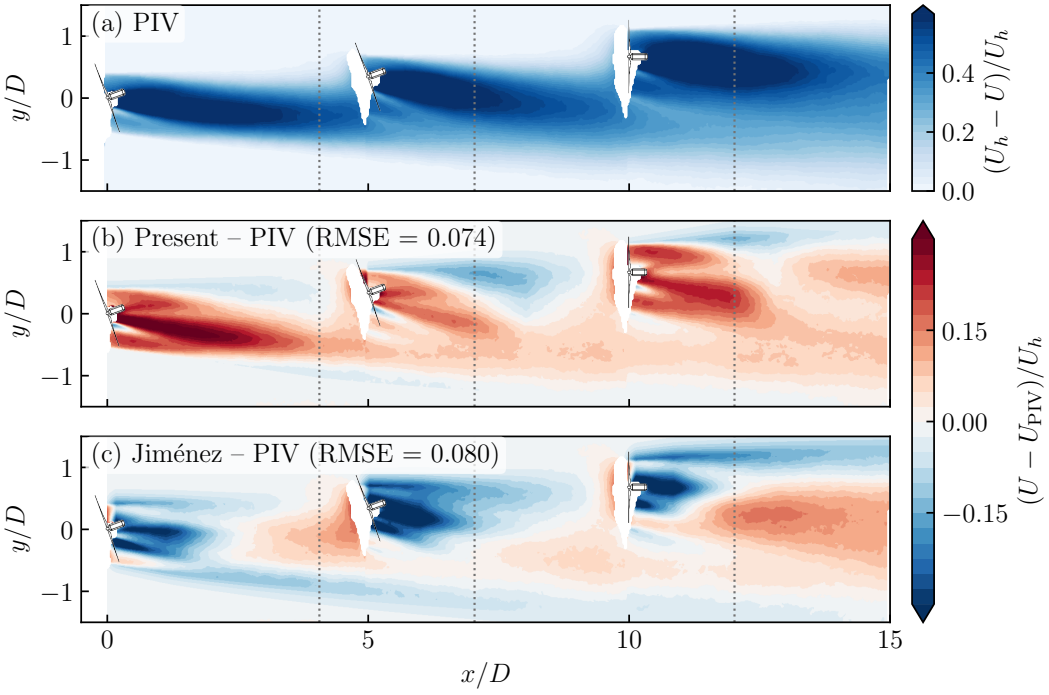

Figure 14. As Fig. 13, for the staggered Case S_1 ($\gamma_1 = -20°$, $\gamma_2 = -20°$, $\gamma_3 = 0°$) – the configuration in which the wake centreline is least well defined. Even here, the field comparison separates the two models: the present model's difference field (b) is smaller and smoother than that of Jiménez et al. (2010) (c).

turbine is unyawed. For the unyawed turbines studied here, these account for 57–66, 31–39 and 3.5–4.2 % of the deflection at the end of the domain, respectively, so over a third of where a wake goes is owed to the rotor's own presence.

The model was evaluated against wind-tunnel PIV measurements for both single- and multi-turbine configurations. In the single-turbine cases, it reproduced the principal features of the streamwise and lateral wakes, with good agreement in the far wake and a lower far-wake deflection error than the model of Bastankhah and Porté-Agel (2016) at every measured yaw angle; both improved on the systematic overprediction of Jiménez et al. (2010). In the three-turbine cases, it reproduced the deflection of the directly yawed wakes and, more importantly, captured secondary wake steering mechanistically – including the deflection of an unyawed downstream rotor, which carries no thrust-driven lateral velocity: its wake is deflected by the upstream cross-flow, and the rotor's own streamwise deficit, by slowing that wake, accounts for about a third of the result. Quantitatively, it returned the lower far-wake deflection error than the Jiménez et al. (2010) baseline in four of the seven three-turbine configurations, tying one and losing two, one of them marginally (Fig. 11); assessed over the full hub-height velocity field, which requires no fitted centreline, it attained the lower error in every configuration (Fig. 12). The main discrepancies are confined to the near wake, where the simplified treatment underpredicts the streamwise velocity deficit; because deflection is a non-local, integrated quantity, this error propagates downstream and is most pronounced for the staggered layouts, where

https://doi.org/10.5194/wes-2026-183
Preprint. Discussion started: 4 November 2026
© Author(s) 2026. CC BY 4.0 License.

eawe european academy of wind energy
Open Access WIND ENERGY SCIENCE DISCUSSIONS

the centreline is least well defined and each rotor sits out on the flank of the upstream wakes (Sect. 4.2.2). That the velocity field set up by upstream wakes can reinforce or suppress the deflection of an internal turbine, depending on the relative lateral positions of the turbines, has also been observed in operational data (Siguenza-Alvarado et al., 2026, Fig. 9).

Whilst the present results are encouraging, several limitations remain that motivate future work:

1. **Near-wake modelling.** The representation of the near wake, where simplified modelling assumptions lead to underprediction of the induced streamwise velocity deficit and discontinuities between the near- and far-wake regimes, should be examined. At the switch, the skew angle of a waked rotor steps by 7–13°, because the near-wake branch of Eq. (29) omits advection. A recent comparison of analytical yaw models by Thompson et al. (2025) found that wake-shape formulations more flexible than the single Gaussian – in particular, double-Gaussian (Keane, 2021) and super-Gaussian (Blondel and Cathelain, 2020) profiles – substantially improve near-wake predictions for yawed turbines. Future work could therefore focus on developing a unified wake-shape formulation based on such flexible functional forms and accounting for pressure variations in the near wake (Bastankhah et al., 2026), provided it remains analytically integrable within the present momentum-deficit framework.

2. **Lateral wake modelling.** The assumption of an asymmetric Gaussian profile may not be appropriate for small yaw angles, where the profile exhibits both a positive and a negative peak. Its behaviour on the flanks also deserves attention: beyond about 2σ from the lateral wake centre, it captures neither the change of sign of the measured surplus on one side, nor the tail that persists on the other. Neither shortcoming bears on an isolated rotor, whose deflection is evaluated close to the lateral wake centre, but the staggered cases of Sect. 4.2.2 show that both can bear on a rotor positioned out on the flank of an upstream wake, and so on the predicted lateral momentum transport and deflection.

3. **Neglected terms of the governing equation.** As noted by Bastankhah et al. (2021), the applicability of the conservation of momentum deficit equation (Eq. (2)) – now for lateral as well as streamwise momentum – should be investigated for a range of inflow conditions and layout geometries; this study assumes that their budget analysis carries over to the lateral equation. It also bears on the choice of $\alpha = 2$ in Eq. (11): the modified value $\alpha = 1$ of Bastankhah et al. (2021) was proposed as an empirical correction for precisely these neglected terms. Retaining the exact value keeps the streamwise and lateral solutions mutually consistent, at the cost of forgoing any potential compensation; the agreement reported in Sect. 4 suggests the cost is small for the conditions examined here, but this warrants revisiting alongside the budget analysis.

4. **More comprehensive validation.** The current model has primarily been evaluated against idealised wind-tunnel data and requires more comprehensive validation against high-fidelity simulations and full-scale field measurements across a wider range of atmospheric and operational conditions (Bao et al., 2024; Siguenza-Alvarado et al., 2026). In particular, the model's behaviour under various atmospheric stabilities and wind veer remains to be assessed, as does its behaviour in heterogeneous inflow, where two questions separate. Kinematically, a background cross-flow $V_0(x, y, z)$ enters the far-wake branch of Eq. (29) directly, so that as $C_{T,i} \to 0$ the far wake follows the background streamline, although every

https://doi.org/10.5194/wes-2026-183
Preprint. Discussion started: 4 November 2026
© Author(s) 2026. CC BY 4.0 License.

eawe european academy of wind energy
Open Access WIND ENERGY SCIENCE DISCUSSIONS

case here has $V_0 = 0$. Dynamically, the background-gradient terms $U_i\,\partial \boldsymbol{U}_0/\partial x_i$ of Eq. (1) are neglected and the closed-form solutions take $U_0 = U_h$, so the momentum-deficit balance itself is untested where complex terrain or gravity waves make the background flow vary on the scale of the wakes.

5. **Robust, power-relevant validation metrics.** The headline deflection comparison reduces each case to a fitted wake centreline, which becomes ill-defined where wakes merge and is least reliable for the staggered layouts. The hub-height field comparison of Sect. 4.2.3 is a first step towards a metric that needs no centreline and is closer to what matters for power. A fuller assessment should pair a centreline definition that remains robust for merged wakes with directly power-relevant scalars – rotor-effective wind speed and turbine power ratios – validated against operational data from wake-steering campaigns (Siguenza-Alvarado et al., 2026).

Finally, the analytical framework introduced here provides a foundation for future wind farm control and optimisation studies. Because the model predicts lateral velocities directly and maintains a computationally efficient analytical structure, it may prove useful for applications requiring physically interpretable low-order models, including closed-loop wind farm control, layout optimisation, and wind-farm co-design.

Appendix A: Wake widths and lateral wake centre

A1 Streamwise width and far-wake onset

Bastankhah and Porté-Agel (2016) give the lateral and vertical wake widths at the end of the potential core as

$$\frac{\sigma_{y_0}}{D} = \sqrt{\frac{1+\sqrt{1-C_T\cos\gamma}}{8\left(1+\sqrt{1-C_T}\right)}}\cos\gamma, \qquad \frac{\sigma_{z_0}}{D} = \sqrt{\frac{1+\sqrt{1-C_T\cos\gamma}}{8\left(1+\sqrt{1-C_T}\right)}}, \tag{A1}$$

with the subscript 0 denoting, as in Bastankhah and Porté-Agel (2016), the end of the potential core. The self-similar profile of Eq. (9) carries a single width in both directions, so we take the geometric mean,

$$\sigma_0 = \sqrt{\sigma_{y_0}\,\sigma_{z_0}}, \tag{A2}$$

which is the unique isotropic width that leaves the integrated deficit unchanged, since $\int f\,\mathrm{d}A = 2\pi\sigma_y\sigma_z$ for an anisotropic Gaussian and $2\pi\sigma^2$ for an isotropic one. Each component then grows linearly as in Eq. (31), and $I_{\mathrm{local},i}$ adds to the ambient value, in quadrature, the largest added turbulence from the upstream turbines, each contribution given by the turbulence-optimised form of the Crespo and Hernández (1996) correlation of Zehtabiyan-Rezaie et al. (2024, Eq. 8) and weighted by the fraction of the rotor of WT_i inside that turbine's wake (Niayifar and Porté-Agel, 2016). The length of the potential core is that given by Bastankhah and Porté-Agel (2016),

$$\frac{x_{0,i}}{D} = \frac{\cos\gamma_i\left(1+\sqrt{1-C_{T,i}}\right)}{\sqrt{2}\left(\alpha^* I_{\mathrm{local},i} + \beta^*\left(1-\sqrt{1-C_{T,i}}\right)\right)}, \tag{A3}$$

https://doi.org/10.5194/wes-2026-183
Preprint. Discussion started: 4 November 2026
© Author(s) 2026. CC BY 4.0 License.

eawe european academy of wind energy
Open Access WIND ENERGY SCIENCE DISCUSSIONS

where $\alpha^* = 2.32$, $\beta^* = 0.154$. It serves only to position the width line of Eq. (31). The far-wake self-deficit falls monotonically as the wake widens, so the switch of Eq. (28) turns off once. Equating Eq. (10) without its upstream sums to Eq. (25) gives the onset width in closed form,

$$\frac{\sigma_{\ell,i}^2}{D^2} = \frac{\cos\gamma_i}{8}\,\frac{r_i\,(1-a_i)}{1-a_i r_i}, \qquad r_i = \frac{\langle U_{1:i-1}\rangle_{(i,x_i)}}{U_h}, \tag{A4}$$

and inverting Eq. (31) for it is a quadratic, so the onset lies a distance

$$\ell_i = x_{0,i} + \frac{\sqrt{(\sigma_{y_0}-\sigma_{z_0})^2 + 4\sigma_{\ell,i}^2} - (\sigma_{y_0}+\sigma_{z_0})}{2k_U} \tag{A5}$$

downstream of the rotor, at $x_{\chi,i} = x_i + \ell_i$. For a rotor in undisturbed uniform inflow, $r_i = 1$ and Eq. (A4) reduces to $\sigma_\ell = D\sqrt{\cos\gamma/8}$, independent of C_T. This equals σ_0 of Eq. (A2) at zero yaw, so the onset then coincides with the end of the potential core exactly. With yaw it falls 0.11–$0.26D$ upstream of it in the cases considered here, and for a waked rotor, $r_i < 1$, 0.4–$1.2D$ upstream.

A2 Lateral wake centre

Figure A1 tests the approximation of Sect. 3, that $\partial V/\partial y = 0$ where $\partial^2 U/\partial y^2 = 0$, against the experimental data of Bastankhah and Porté-Agel (2016). It holds reasonably well, and best on the side of the wake where the streamwise wake centre lies ($y > 0$), which is where the model applies it.

https://doi.org/10.5194/wes-2026-183
Preprint. Discussion started: 4 November 2026
© Author(s) 2026. CC BY 4.0 License.

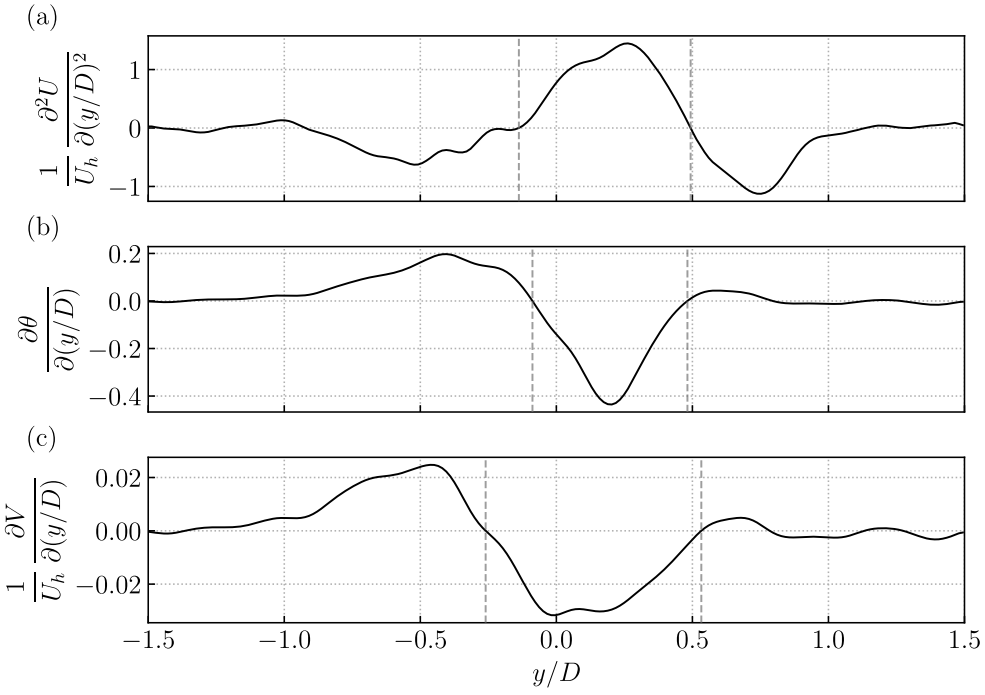

Figure A1. (a) Second derivative of normalised streamwise velocity, (b) first derivative of wake skew angle, and (c) first derivative of normalised lateral velocity with respect to lateral coordinate at a downstream distance of $x/D = 3.0$ for a turbine operating at a yaw angle of $\gamma = 20°$. Dashed grey lines show the location of the zero-crossing closest to $y = 0$ on each side.

A3 Deflection-side onset width

At the far-wake onset, the near-wake solution is given at the streamwise wake centre, which is not co-located with the lateral wake centre; by Eq. (16), the lateral velocity there depends only on the deflection-side width τ_{A_ℓ}. For a single turbine, evaluated at the hub height z_h, Eq. (7) gives

$$\frac{V_\ell}{U_h} = \frac{V_0}{U_h} - \frac{\Delta\tilde{V}_\ell}{U_h}\, g_\ell\,(y = \delta, z = z_h), \tag{A6}$$

with $g_\ell(y = \delta, z = z_h) = \exp(-\sigma_\ell^2/2\tau_{A_\ell}^2)$ from Eq. (16) and, from Eq. (18),

$$\frac{\Delta\tilde{V}_\ell}{U_h} = \frac{-\left(\frac{C_T}{8}\right)\sin\gamma}{\left(\frac{\tau_{A_\ell}}{D}\right)^2 + \left(\frac{\tau_{B_\ell}}{D}\right)^2 - \frac{\Delta\tilde{U}_\ell}{U_h}\left(\frac{\sigma_\ell}{D}\right)^2 \nu_\ell}, \tag{A7}$$

with

$$\nu_\ell = \left[1 + \mathrm{erf}\left(\frac{\tau_{A_\ell}}{\sqrt{2\left(\sigma_\ell^2 + \tau_{A_\ell}^2\right)}}\right)\right] \frac{\tau_{A_\ell}^2}{\sigma_\ell^2 + \tau_{A_\ell}^2} \exp\left(-\frac{\sigma_\ell^2}{2\left(\sigma_\ell^2 + \tau_{A_\ell}^2\right)}\right) + \left[1 - \mathrm{erf}\left(\frac{\tau_{B_\ell}}{\sqrt{2\left(\sigma_\ell^2 + \tau_{B_\ell}^2\right)}}\right)\right] \frac{\tau_{B_\ell}^2}{\sigma_\ell^2 + \tau_{B_\ell}^2} \exp\left(-\frac{\sigma_\ell^2}{2\left(\sigma_\ell^2 + \tau_{B_\ell}^2\right)}\right).$$

https://doi.org/10.5194/wes-2026-183
Preprint. Discussion started: 4 November 2026
© Author(s) 2026. CC BY 4.0 License.

eawe european academy of wind energy
Open Access WIND ENERGY SCIENCE DISCUSSIONS

(A8)

This has two unknowns, $\Delta\tilde{V}_\ell$ and τ_{A_ℓ}. The first is given by Eq. (27); the second requires a skew angle independent of the present model's own lateral velocity, since Eq. (24) evaluated with Eq. (27) would merely return the near-wake solution and determine nothing. We therefore take θ_{c_0} of Eq. (34) as the skew angle at the onset: the potential core of Bastankhah and Porté-Agel (2016) ends at $x_i + x_{0,i}$, which for a rotor in uniform inflow coincides with the onset at zero yaw and lies within about a quarter of a diameter of it in yaw (Eq. (A5)). Consistent with this, and assuming $\langle U_0 \rangle = U_h$, the streamwise velocity at the streamwise wake centre is taken from the same potential-core solution, Eq. (25), giving $\Delta\tilde{U}_\ell/U_h = 2a$. The skew angle at the far-wake onset is then

$$\theta_\ell = \frac{V_\ell}{U_h - \Delta\tilde{U}_\ell} = \frac{V_0 - \Delta\tilde{V}_\ell \exp\left(-\frac{\sigma_\ell^2}{2\tau_{A_\ell}^2}\right)}{U_h - \Delta\tilde{U}_\ell}, \tag{A9}$$

in which the only far-wake quantity is the Gaussian factor that attenuates the peak $\Delta\tilde{V}_\ell$ to its value at the streamwise wake centre. Solving for τ_{A_ℓ},

$$\frac{\tau_{A_\ell}}{D} = \frac{\frac{\sigma_\ell}{D}}{\sqrt{2\ln\left(\frac{\Delta\tilde{V}_\ell}{V_0 - \theta_\ell(U_h - \Delta\tilde{U}_\ell)}\right)}}, \tag{A10}$$

and substituting $\theta_\ell = \theta_{c_0}$, $V_0 = 0$ and the near-wake solutions of Eqs. (27) and (25) gives Eq. (35).

A4 Non-deflection-side onset width

Equating Eq. (A7) with Eq. (27) and substituting Eq. (25) gives

$$\left(\frac{\tau_{A_\ell}}{D}\right)^2 + \left(\frac{\tau_{B_\ell}}{D}\right)^2 - 2a\left(\frac{\sigma_\ell}{D}\right)^2 \nu_\ell - \frac{1}{2} = 0, \tag{A11}$$

which has no closed-form solution for τ_{B_ℓ}, since ν_ℓ is itself a function of it, and would have to be solved iteratively for every turbine.

https://doi.org/10.5194/wes-2026-183
Preprint. Discussion started: 4 November 2026
© Author(s) 2026. CC BY 4.0 License.

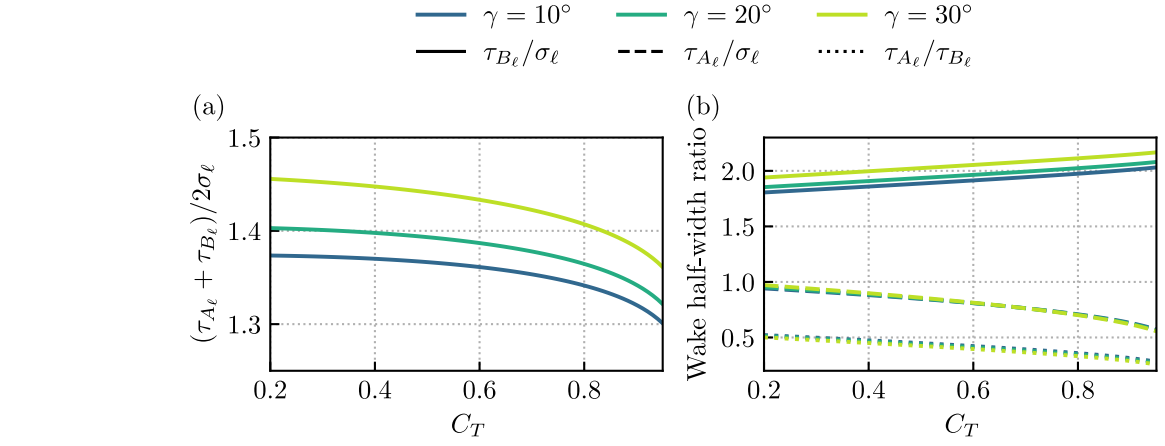

Figure A2. Variation in (a) the ratio of lateral wake width to streamwise wake width, and (b) various characteristic wake width ratios at the far-wake onset, over a range of values of thrust coefficient.

Figure A2 shows the onset widths over $0.2 \leq C_T \leq 0.95$ – the windmill state assumed by Bastankhah and Porté-Agel (2016), from whom the onset relations derive – with σ_ℓ, τ_{A_ℓ} and τ_{B_ℓ} from Eqs. (A4), (35) and (A11). The ratio $(\tau_{A_\ell} + \tau_{B_\ell})/2\sigma_\ell$ varies by at most about $7\,\%$ (panel a), supporting $2\sigma \propto (\tau_A + \tau_B)$. The half-widths differ (panel b): τ_{B_ℓ} departs from $2\sigma_\ell$ by at most about $10\,\%$, whereas τ_{A_ℓ} falls by as much as $43\,\%$, from $0.97\sigma_\ell$ at $C_T = 0.2$ to $0.56\sigma_\ell$ at $C_T = 0.95$ for $\gamma = 30°$, passing $0.75\sigma_\ell$ near $C_T \approx 0.72$. Fixing τ_{B_ℓ} therefore costs at most that $10\,\%$, whereas fixing τ_{A_ℓ} would introduce a systematic, C_T-dependent error in the predicted deflection away from $C_T \approx 0.72$.

Appendix B: Implementation

Algorithm B1 summarises the model in the order in which it is computed.

Algorithm B1. Analytical wake steering model

1: **Input:** turbine set $\{(x_i, y_i, z_i, D, \gamma_i)\}_{i=1}^{n}$, provided in upstream-to-downstream order
2: **Input:** inflow quantities (U_h, V_h, I_0) [with $V_h \equiv V_0|_{z=z_h}$] and computational grid (x, y, z)
3: **Allocate:** arrays $\sigma, \tau_A, \tau_B, \delta, \epsilon, \theta, \Delta\tilde{U}, \Delta\tilde{V}$, and the deflection components $\delta^{\mathrm{tr}}, \delta^{\mathrm{car}}, \delta^{\mathrm{thr}}, \delta^{\mathrm{inh}}$
4: **for** each turbine $i = 1, \ldots, n$ **do**
5: Evaluate the flow of turbines $1, \ldots, i-1$ (Eq. (7)) analytically at quadrature points on the rotor disc of WT_i, giving the rotor-averaged streamwise velocity $\langle U_{1:i-1} \rangle_{(i,x_i)}$ of Eq. (3) and the hub lateral velocity $V_{\mathrm{local},i}$ of Eq. (17)
6: Compute thrust coefficient C_{T_i} (Zong and Porté-Agel, 2021, Eq. 12), then induction a_i (Eq. (26)), and the deflection-side sign s_i (Eq. (17))

https://doi.org/10.5194/wes-2026-183
Preprint. Discussion started: 4 November 2026
© Author(s) 2026. CC BY 4.0 License.

eawe european academy of wind energy
Open Access WIND ENERGY SCIENCE DISCUSSIONS

Compute near-wake reference values $\Delta\tilde{U}_{i,\mathrm{nw}}$ (Eq. (25)) and $\Delta\tilde{V}_{i,\mathrm{nw}}$ (Eq. (27))

Compute the local turbulence intensity $I_{\mathrm{local},i}$ and the growth rate $k_{U,i}$ as in Sect. 3, taking the largest added turbulence over the upstream turbines, each weighted by the fraction of the rotor of WT_i inside that wake

Compute the potential-core length $x_{0,i}$ (Eq. (A3)) and the widths $\sigma_{y_0,i}, \sigma_{z_0,i}$ there (Eq. (A1)); build $\sigma_i(x)$ for $x \geq x_i$ from Eq. (31)

Compute the far-wake onset width $\sigma_{\ell,i}$ (Eq. (A4)) and its station $x_{\chi,i} = x_i + \ell_i$ (Eq. (A5))

Evaluate $\tau_{A,\ell,i}$ in closed form (Eq. (35)) and set $\tau_{B,\ell,i} = 2\,\sigma_{\ell,i}$

Set $k_{V_B,i} = k_{U,i}$ and $k_{V_A,i} = (\tau_{A,\ell,i}/\tau_{B,\ell,i})\,k_{U,i}$ (Eq. (36))

Build $\tau_{Ai}(x)$ and $\tau_{Bi}(x)$ growing linearly from their onset values at $x_{\chi,i}$; upstream of $x_{\chi,i}$, ramp linearly from $\tau_{A\phi_i} = (\tau_{A,\ell,i}/\sigma_{\ell,i})\sigma_{\phi_i}$ and $\tau_{B\phi_i} = 2\sigma_{\phi_i}$ at the rotor, where $\sigma_{\phi_i} = \sigma_i(x_i)$

for each streamwise index j such that $x_j \geq x_i$ and $j < n_x - 1$ **do**

  Set the lateral wake centre $\epsilon_{i,j} = \delta_{i,j} - s_i\,\sigma_{i,j}$ (Eq. (32)), which μ_{ii} requires

  Build upstream interaction terms λ_{ij} (Eq. (11)) and μ_{ij}, μ_{ji} (Eq. (20)) from turbines $1, \ldots, i-1$ at x_j

  Compute $\Delta\tilde{U}^{\mathrm{self}}_{i,j}$, the single-turbine balance with the farm's inputs, i.e. Eq. (10) without the upstream sums

  Evaluate the near-wake switch $\chi^{\mathrm{nw}}_{i,j}$ (Eq. (28)), i.e. whether $\Delta\tilde{U}^{\mathrm{self}}_{i,j} > \Delta\tilde{U}_{i,\mathrm{nw}}$ at $x_j \geq x_i$

  if $\chi^{\mathrm{nw}}_{i,j}$ **then**

    Cap the turbine alone at the near-wake values:

$$\Delta\tilde{U}_{i,j} \leftarrow \min\left(\Delta\tilde{U}^{\mathrm{self}}_{i,j}, \Delta\tilde{U}_{i,\mathrm{nw}}\right), \qquad \Delta\tilde{U}^{\mathrm{int}}_{i,j} \leftarrow 0$$

    Compute $\Delta\tilde{V}_{i,j}$ from Eq. (18) without either upstream sum, capped in magnitude at $|\Delta\tilde{V}_{i,\mathrm{nw}}|$; set $\Delta\tilde{V}^{\mathrm{thr}}_{i,j} \leftarrow \Delta\tilde{V}_{i,j}$ and $\Delta\tilde{V}^{\mathrm{inh}}_{i,j} \leftarrow 0$

    Evaluate $\theta_{i,j}$ from the near-wake branch of Eq. (29); set $\theta^{\mathrm{thr}}_{i,j} \leftarrow \theta_{i,j}$ and $\theta^{\mathrm{tr}}_{i,j} = \theta^{\mathrm{car}}_{i,j} = \theta^{\mathrm{inh}}_{i,j} \leftarrow 0$

  else

    Compute $\Delta\tilde{U}_{i,j}$ from Eq. (10), capped at $\Delta\tilde{U}_{i,\mathrm{nw}}$, and $\Delta\tilde{U}^{\mathrm{int}}_{i,j} = \Delta\tilde{U}_{i,j} - \Delta\tilde{U}^{\mathrm{self}}_{i,j}$

    Compute $\Delta\tilde{V}_{i,j}$ from Eq. (18), and its thrust-driven and inherited components from Eqs. (21) and (22)

    Sample the flow of turbines $1, \ldots, i-1$ at the wake centreline $(x_j,\, y_i + \delta_{i,j},\, z_i)$, giving U_i^{up} and V_i^{up}

    Evaluate $\theta_{i,j}$ from the far-wake branch of Eq. (29), and its components $\theta^{\mathrm{tr}}_{i,j}, \theta^{\mathrm{car}}_{i,j}, \theta^{\mathrm{thr}}_{i,j}, \theta^{\mathrm{inh}}_{i,j}$ from Eq. (30)

  end if

  Update the wake-centre deflection and each of its components $c \in \{\mathrm{tr}, \mathrm{car}, \mathrm{thr}, \mathrm{inh}\}$ (forward Euler):

$$\delta_{i,j+1} \leftarrow \delta_{i,j} + \theta_{i,j}\,(x_{j+1} - x_j), \qquad \delta^c_{i,j+1} \leftarrow \delta^c_{i,j} + \theta^c_{i,j}\,(x_{j+1} - x_j), \qquad \delta_i(x_i) = \delta^c_i(x_i) = 0$$

end for

https://doi.org/10.5194/wes-2026-183
Preprint. Discussion started: 4 November 2026
© Author(s) 2026. CC BY 4.0 License.

eawe european academy of wind energy
Open Access WIND ENERGY SCIENCE DISCUSSIONS

31: (Optional, for the velocity field only.) Apply the wake of WT_i downstream, with streamwise shape f_i (Eq. (9)) and lateral shape g_i (Eq. (16)), its side selected pointwise by s_i:

$$U \leftarrow U - \Delta\tilde{U}_i f_i, \qquad V \leftarrow V - \Delta\tilde{V}_i g_i, \qquad \text{starting from } U = U_0,\ V = V_0$$

32: **end for**

Appendix C: Sensitivity of the Jiménez et al. (2010) baseline to the superposition rule and the spreading rate

The baseline combines its wakes by a rule chosen on its behalf. The present model also sums its wake deficits (Eq. (7)), but the amplitude of each follows from the momentum-deficit balance with the wakes upstream of it, so there is no rule to choose. Table C1 repeats the field comparison of Sect. 4.2.3 under four superposition rules, with the deflection, deficit and turbulence models and the thrust coefficient held fixed.

Table C1. Sensitivity of the hub-height field comparison to the wake superposition used in the Jiménez et al. (2010) baseline: the RMSE of U/U_h over the far-wake region of the common PIV domain, as in Sect. 4.2.3. Only the superposition differs: linear summation of ambient-scaled deficits (as used throughout the paper), squared summation, linear summation of deficits scaled by the local inflow (Niayifar and Porté-Agel, 2016), and the momentum-conserving superposition of Zong and Porté-Agel (2020). The present model attains the lowest error in every case under every variant except Case S_1 under the momentum-conserving superposition, a dead heat. Lower is better.

	Present	Jiménez et al. (2010) baseline			
Case	model	Linear sum	Squared sum	Local-inflow linear	Momentum-conserving
A_0	**0.039**	0.083	0.060	0.046	0.070
A_1	**0.052**	0.087	0.084	0.064	0.077
A_2	**0.045**	0.092	0.078	0.063	0.079
A_3	**0.048**	0.086	0.078	0.061	0.071
A_4	**0.047**	0.092	0.075	0.065	0.073
S_0	**0.054**	0.083	0.094	0.069	0.068
S_1	0.067	0.084	0.101	0.076	0.067
Mean	**0.050**	0.087	0.081	0.064	0.072

The deflection law of the baseline has a fixed spreading rate, $\beta = 0.1$, which corresponds through $k^* = 0.38I + 0.004$ to $I \approx 25\,\%$, some three times the turbulence intensities of the experiments considered here. Tying it to the local turbulence intensity instead worsens the overprediction: the mean far-wake deflection error rises from $0.198D$ to $0.394D$ over the yawed single-turbine cases ($10°$–$30°$), and from $0.056D$ to $0.071D$ over the three-turbine cases.

https://doi.org/10.5194/wes-2026-183
Preprint. Discussion started: 4 November 2026
© Author(s) 2026. CC BY 4.0 License.

eawe european academy of wind energy
Open Access WIND ENERGY SCIENCE DISCUSSIONS

Code and data availability. The Python implementation of the model and the scripts to reproduce the simulations and figures are archived at https://doi.org/10.5281/zenodo.23206868 (Gaukroger and Siguenza-Alvarado, 2026) (version v1.0.1) and developed at https://gitlab.windenergy.dtu.dk/njoga/awsmf (MIT Licence). The experimental PIV data of Bastankhah and Porté-Agel (2020) are openly available at https://doi.org/10.5281/zenodo.3607598; the wake deflection and centreline-deficit curves used here are derived directly from those fields by the reproduction scripts. The numerical comparison data of Zong and Porté-Agel (2020, 2021) were provided directly by the authors and are used with their permission; they are not redistributed here and will be made available by the authors through their own repository. Neither third-party dataset is included in the software archive; reproducers must obtain them as described in the repository (`data/third_party/`).

Author contributions. N.J.G.: derived the model from the governing equations, developed and implemented the Python code, coordinated the collaboration and meetings, and led the manuscript preparation, including substantial writing, restructuring, and figure development. D.S.-A.: contributed to model development and numerical implementation, as well as manuscript drafting and revision. M.P.v.d.L.: contributed to model development discussions, provided an external perspective on implementation and validation, and contributed to critical revision of the manuscript. M.B.: proposed the original extension of the momentum-conserving formulation to include lateral momentum for yawed turbines, conceived the asymmetric Gaussian formulation for the lateral velocity and contributed to the theoretical development throughout the project. All authors contributed to discussions on the model development and revised the manuscript.

Competing interests. At least one of the (co-)authors is a member of the editorial board of Wind Energy Science. The authors have no other competing interests to declare.

Acknowledgements. The authors would like to thank Haohua Zong and Fernando Porté-Agel for providing their results for us to plot directly, and Pierre-Elouan Réthoré for his comments on the manuscript. The authors are also grateful to the European Wind Energy Master's, an Erasmus Mundus programme of the EU, for providing the framework to begin this work as part of N.J.G.'s master's thesis. The authors acknowledge the use of generative artificial intelligence tools to assist with the writing process and to develop the model and post-processing code for producing figures. All scientific content, analysis, and conclusions remain the responsibility of the authors.

Financial support. This research has been supported by Equinor ASA through an academic collaboration agreement with the Technical University of Denmark. The contribution of D.S.-A. has been supported by the Engineering and Physical Sciences Research Council through the Impact Acceleration Account at Durham University (grant no. EP/Y024052/1).

https://doi.org/10.5194/wes-2026-183
Preprint. Discussion started: 4 November 2026
© Author(s) 2026. CC BY 4.0 License.

eawe european academy of wind energy
Open Access WIND ENERGY SCIENCE DISCUSSIONS

References

Allaerts, D. and Meyers, J.: Boundary-Layer Development and Gravity Waves in Conventionally Neutral Wind Farms, J. Fluid Mech., 814, 95–130, https://doi.org/10.1017/jfm.2017.11, 2017.

Bao, T., Li, Z., Li, Y., Pan, Y., Chan, R. W. K., Pu, O., Huang, B., Yan, K., Peng, B., and Wu, H.: Wake Measurement of Wind Turbine under Yawed Conditions Using UAV Anemometry System, J. Wind Eng. Ind. Aerodyn., 249, 105 720, https://doi.org/10.1016/j.jweia.2024.105720, 2024.

Bastankhah, M. and Porté-Agel, F.: Experimental and Theoretical Study of Wind Turbine Wakes in Yawed Conditions, J. Fluid Mech., 806, 506–541, https://doi.org/10.1017/jfm.2016.595, 2016.

Bastankhah, M. and Porté-Agel, F.: Wind Tunnel Study of the Wind Turbine Interaction with a Boundary-Layer Flow: Upwind Region, Turbine Performance, and Wake Region, Phys. Fluids, 29, 065 105, https://doi.org/10.1063/1.4984078, 2017.

Bastankhah, M. and Porté-Agel, F.: Experimental and Theoretical Study of Wind Turbine Wakes in Yawed Conditions, Zenodo [data set], https://doi.org/10.5281/zenodo.3607598, 2020.

Bastankhah, M., Welch, B. L., Martínez-Tossas, L. A., King, J., and Fleming, P.: Analytical Solution for the Cumulative Wake of Wind Turbines in Wind Farms, J. Fluid Mech., 911, A53, https://doi.org/10.1017/jfm.2020.1037, 2021.

Bastankhah, M., Shapiro, C. R., Shamsoddin, S., Gayme, D. F., and Meneveau, C.: A Vortex Sheet Based Analytical Model of the Curled Wake behind Yawed Wind Turbines, J. Fluid Mech., 933, A2, https://doi.org/10.1017/jfm.2021.1010, 2022.

Bastankhah, M., Hydon, P., Shapiro, C., Gayme, D., and Meneveau, C.: Generalised Actuator Disk Theory: Wake Development with Turbulent Entrainment, J. Fluid Mech., 1039, A29, https://doi.org/10.1017/jfm.2026.11732, 2026.

Bay, C. J., Fleming, P., Doekemeijer, B., King, J., Churchfield, M., and Mudafort, R.: Addressing Deep Array Effects and Impacts to Wake Steering with the Cumulative-Curl Wake Model, Wind Energy Sci., 8, 401–419, https://doi.org/10.5194/wes-8-401-2023, 2023.

Blondel, F. and Cathelain, M.: An Alternative Form of the Super-Gaussian Wind Turbine Wake Model, Wind Energy Sci., 5, 1225–1236, https://doi.org/10.5194/wes-5-1225-2020, 2020.

Brugger, P., Debnath, M., Scholbrock, A., Fleming, P., Moriarty, P., Simley, E., Jager, D., Roadman, J., Murphy, M., Zong, H., and Porté-Agel, F.: Lidar Measurements of Yawed-Wind-Turbine Wakes: Characterization and Validation of Analytical Models, Wind Energy Sci., 5, 1253–1272, https://doi.org/10.5194/wes-5-1253-2020, 2020.

Crespo, A. and Hernández, J.: Turbulence Characteristics in Wind-Turbine Wakes, J. Wind Eng. Ind. Aerodyn., 61, 71–85, https://doi.org/10.1016/0167-6105(95)00033-X, 1996.

Crespo, A., Hernández, J., and Frandsen, S.: Survey of Modelling Methods for Wind Turbine Wakes and Wind Farms, Wind Energy, 2, 1–24, https://doi.org/10.1002/(SICI)1099-1824(199901/03)2:1<1::AID-WE16>3.0.CO;2-7, 1999.

Fleming, P., Annoni, J., Shah, J. J., Wang, L., Ananthan, S., Zhang, Z., Hutchings, K., Wang, P., Chen, W., and Chen, L.: Field Test of Wake Steering at an Offshore Wind Farm, Wind Energy Sci., 2, 229–239, https://doi.org/10.5194/wes-2-229-2017, 2017.

Fleming, P., Annoni, J., Churchfield, M., Martínez-Tossas, L. A., Gruchalla, K., Lawson, M., and Moriarty, P.: A Simulation Study Demonstrating the Importance of Large-Scale Trailing Vortices in Wake Steering, Wind Energy Sci., 3, 243–255, https://doi.org/10.5194/wes-3-243-2018, 2018.

Gaukroger, N. J. and Siguenza-Alvarado, D.: An Analytical Wake Deflection Model for Wind Farms Including Secondary Wake Steering, Zenodo [code], https://doi.org/10.5281/zenodo.23206868, 2026.

https://doi.org/10.5194/wes-2026-183
Preprint. Discussion started: 4 November 2026
© Author(s) 2026. CC BY 4.0 License.

Gebraad, P. M. O., Teeuwisse, F. W., van Wingerden, J. W., Fleming, P. A., Ruben, S. D., Marden, J. R., and Pao, L. Y.: Wind Plant Power Optimization through Yaw Control Using a Parametric Model for Wake Effects-a CFD Simulation Study, Wind Energy, 19, 95–114, https://doi.org/10.1002/we.1822, 2016.

Howland, M. F., Bossuyt, J., Martínez-Tossas, L. A., Meyers, J., and Meneveau, C.: Wake Structure in Actuator Disk Models of Wind Turbines in Yaw under Uniform Inflow Conditions, J. Renew. Sustain. Energy, 8, 043 301, https://doi.org/10.1063/1.4955091, 2016.

Jiménez, Á., Crespo, A., and Migoya, E.: Application of a LES Technique to Characterize the Wake Deflection of a Wind Turbine in Yaw, Wind Energy, 13, 559–572, https://doi.org/10.1002/we.380, 2010.

Keane, A.: Advancement of an Analytical Double-Gaussian Full Wind Turbine Wake Model, Renew. Energy, 171, 687–708, https://doi.org/10.1016/j.renene.2021.02.078, 2021.

King, J., Fleming, P., King, R., Martínez-Tossas, L. A., Bay, C. J., Mudafort, R., and Simley, E.: Control-Oriented Model for Secondary Effects of Wake Steering, Wind Energy Sci., 6, 701–714, https://doi.org/10.5194/wes-6-701-2021, 2021.

Lignarolo, L. E., Ragni, D., Krishnaswami, C., Chen, Q., Simão Ferreira, C. J., and van Bussel, G. J.: Experimental Analysis of the Wake of a Horizontal-Axis Wind-Turbine Model, Renew. Energy, 70, 31–46, https://doi.org/10.1016/j.renene.2014.01.020, 2014.

Martínez-Tossas, L. A., Annoni, J., Fleming, P. A., and Churchfield, M. J.: The Aerodynamics of the Curled Wake: A Simplified Model in View of Flow Control, Wind Energy Sci., 4, 127–138, https://doi.org/10.5194/wes-4-127-2019, 2019.

Meneveau, C.: Big Wind Power: Seven Questions for Turbulence Research, J. Turbul., 20, 2–20, https://doi.org/10.1080/14685248.2019.1584664, 2019.

Niayifar, A. and Porté-Agel, F.: Analytical Modeling of Wind Farms: A New Approach for Power Prediction, Energies, 9, 741, https://doi.org/10.3390/en9090741, 2016.

Pedersen, M. M., van der Laan, P., Friis-Møller, M., Forsting, A. M., Riva, R., Romàn, L. A. A., Risco, J. C., Quick, J., Christiansen, J. P. S., Olsen, B. T., Rodrigues, R. V., and Réthoré, P.-E.: DTUWindEnergy/PyWake: PyWake, Zenodo [code], https://doi.org/10.5281/zenodo.2562661, 2023.

Peña, A., Schaldemose Hansen, K., Ott, S., and van der Laan, M. P.: On Wake Modeling, Wind-Farm Gradients, and AEP Predictions at the Anholt Wind Farm, Wind Energy Sci., 3, 191–202, https://doi.org/10.5194/wes-3-191-2018, 2018.

Politis, E. S., Prospathopoulos, J., Cabezon, D., Hansen, K. S., Chaviaropoulos, P. K., and Barthelmie, R. J.: Modeling Wake Effects in Large Wind Farms in Complex Terrain: The Problem, the Methods and the Issues, Wind Energy, 15, 161–182, https://doi.org/10.1002/we.481, 2012.

Porté-Agel, F., Bastankhah, M., and Shamsoddin, S.: Wind-Turbine and Wind-Farm Flows: A Review, Bound.-Layer Meteorol., 174, 1–59, https://doi.org/10.1007/s10546-019-00473-0, 2020.

Qian, G.-W. and Ishihara, T.: A New Analytical Wake Model for Yawed Wind Turbines, Energies, 11, 665, https://doi.org/10.3390/en11030665, 2018.

Reinwardt, I., Schilling, L., Steudel, D., Dimitrov, N., Dalhoff, P., and Breuer, M.: Validation of the Dynamic Wake Meandering Model with Respect to Loads and Power Production, Wind Energy Sci., 6, 441–460, https://doi.org/10.5194/wes-6-441-2021, 2021.

Schneemann, J., Rott, A., Dörenkämper, M., Steinfeld, G., and Kühn, M.: Cluster Wakes Impact on a Far-Distant Offshore Wind Farm's Power, Wind Energy Sci., 5, 29–49, https://doi.org/10.5194/wes-5-29-2020, 2020.

Shapiro, C. R., Gayme, D. F., and Meneveau, C.: Modelling Yawed Wind Turbine Wakes: A Lifting Line Approach, J. Fluid Mech., 841, R1, https://doi.org/10.1017/jfm.2018.75, 2018.

https://doi.org/10.5194/wes-2026-183
Preprint. Discussion started: 4 November 2026
© Author(s) 2026. CC BY 4.0 License.

Siguenza-Alvarado, D., Harrison, M., Mohammadi, M., Vishwakarma, P., Bossanyi, E., Landberg, L., and Bastankhah, M.: Assessing Engineering Wake Models Against Operational Data: Insights From the Lillgrund Wind Farm Wake Steering Campaign, Wind Energy, 29, e70 126, https://doi.org/10.1002/we.70126, 2026.

Steiner, J., Hodgson, E. L., van der Laan, M. P., Alcayaga, L., Pedersen, M., Andersen, S. J., Larsen, G., and Réthoré, P.-E.: A Multi-Fidelity Model Intercomparison for Wake Steering of a Large Turbine in a Conventionally Neutral Atmospheric Boundary Layer, Wind Energy Sci., 11, 1679–1703, https://doi.org/10.5194/wes-11-1679-2026, 2026.

Thompson, C., Gouder, K., and Graham, J. M.: Analytical Yaw Models: A Two-Dimensional Comparison, Wind Energy Sci. Discuss. Prepr., https://doi.org/10.5194/wes-2025-218, 2025.

Thomsen, K. and Sørensen, P.: Fatigue Loads for Wind Turbines Operating in Wakes, J. Wind Eng. Ind. Aerodyn., 80, 121–136, https://doi.org/10.1016/S0167-6105(98)00194-9, 1999.

van der Laan, M. P., Meyer Forsting, A., and Réthoré, P.-E.: A Consistent Computational Fluid Dynamics Surrogate Model for Wind Turbine Interaction Including Atmospheric Stability, Wind Energy Sci., 11, 2647–2668, https://doi.org/10.5194/wes-11-2647-2026, 2026.

Vollmer, L., Steinfeld, G., Heinemann, D., and Kühn, M.: Estimating the Wake Deflection Downstream of a Wind Turbine in Different Atmospheric Stabilities: An LES Study, Wind Energy Sci., 1, 129–141, https://doi.org/10.5194/wes-1-129-2016, 2016.

Zehtabiyan-Rezaie, N., Justsen, J. P., and Abkar, M.: Wind-Farm Power Prediction Using a Turbulence-Optimized Gaussian Wake Model, Wind Energy Eng. Res., 2, 100 007, https://doi.org/10.1016/j.weer.2024.100007, 2024.

Zong, H. and Porté-Agel, F.: A Momentum-Conserving Wake Superposition Method for Wind Farm Power Prediction, J. Fluid Mech., 889, A8, https://doi.org/10.1017/jfm.2020.77, 2020.

Zong, H. and Porté-Agel, F.: Experimental Investigation and Analytical Modelling of Active Yaw Control for Wind Farm Power Optimization, Renew. Energy, 170, 1228–1244, https://doi.org/10.1016/j.renene.2021.02.059, 2021.